When White Dwarfs Collide

by

Wendy Phyllis Hawley

A Dissertation Presented in Partial Fulfillment
of the Requirements for the Degree
Doctor of Philosophy

Approved November 2012 by the
Graduate Supervisory Committee:

Frank Timmes, Chair
Patrick Young
Sumner Starrfield
Jennifer Patience
Matt Fouch

ARIZONA STATE UNIVERSITY

December 2012

ABSTRACT

3D models of white dwarf collisions are used to assess the likelihood of double-degenerate mergers as progenitors for Type Ia supernovae (henceforth SNIa) and to identify observational signatures of double-degenerate collisions. Observations of individual SNIa, SNIa rates in different galaxy types, and double white dwarf binary systems suggest that mergers or collisions between two white dwarfs play a role in the overall SNIa population. Given the possibility of two progenitor systems (single-degenerate and double-degenerate), the sample of SNIa used in cosmological calculations needs to be carefully examined. To improve calculations of cosmological parameters, the development of calibrated diagnostics for double-degenerate progenitor SNIa is essential. Head-on white dwarf collision simulations are used to provide an upper limit on the ^{56}Ni production in white dwarf collisions. In chapter II, I explore zero impact parameter collisions of white dwarfs using the Eulerian grid code FLASH. The initial 1D white dwarf profiles are created assuming hydrostatic equilibrium and a uniform composition of 50% ^{12}C and 50% ^{16}O. The masses range from 0.64 to 0.81 $M_{\odot}$ and have an isothermal temperature of 10^7 K. I map these 1D models onto a 3D grid, where the dimensions of the grid are each eight times the white dwarf radius, and the dwarfs are initially placed four white dwarf radii apart (center to center). To provide insight into a larger range of physical possibilities, I also model non-zero impact parameter white dwarf collisions (Chapter III). Although head-on white dwarf collisions provide an upper limit on ^{56}Ni production, non-zero impact parameter collisions provide insight into a wider range of physical scenarios. The initial conditions (box size, initial separation, composition, and initial temperature) are identical to those used for the head-on collisions (Chapter II) for the same range of masses. For each mass pairing, collision simulations are carried out at impact parameters b=1 and b=2 (grazing). Finally, I will address future work to be performed (Chapter IV).

For Frances Hawley

ACKNOWLEDGEMENTS

This work was supported by the National Science Foundation under grant AST 08-06720 and through the Joint Institute for Nuclear Astrophysics (JINA) under grant PHY 02-16783. All simulations were conducted with Arizona State University Advanced Computing Center and Extreme Science and Engineering Discovery Environment (XSEDE) compute resources. FLASH was in part developed by the DOE-supported ASC/Alliances Center for Astrophysical Thermonuclear Flashes at the University of Chicago.

TABLE OF CONTENTS

LIST OF TABLES

LIST OF FIGURES

Chapter 1

INTRODUCTION

Type Ia supernovae (SNIa) play an integral role in cosmology and astrophysics. They are the biggest thermonuclear explosions in the universe, synthesize about half of the iron-group elements in the solar system (Wheeler et al. 1989; Timmes et al. 1995; Feltzing et al. 2001; Strigari 2006), and provide evidence of the accelerated expansion of the universe (Riess et al. 1998). To improve cosmological calculations that use SNIa as distance indicators, an extensive understanding of SNIa progenitor properties is essential.

Supernovae are classified by their spectral signatures, with SNIa lacking prominent hydrogen lines and displaying a strong silicon feature (da Silva 1993). Fig. 1.1 shows the spectra of three SNIa about one week after maximum light. Rest wavelength is on the x-axis and absolute magnitude plus a constant is on the y-axis. The identifying lines are of the neutral or singly ionized intermediate mass elements such as Si II, Ca II, S II, and O I. As shown in the diagram, the spectra of SNIa are quite similar at one week after maximum light for these features (Filippenko et al. 1992).

SNIa are the result of the explosion of at least one white dwarf star. A white dwarf star is the remnant of a low mass main sequence star that has exhausted its nuclear fuel. A low mass main sequence star expels its outer layers at the end of its main sequence lifetime and creates a planetary nebula, leaving behind a hot core. White dwarfs are made of very dense, electron degenerate matter. They are about the size of the Earth, but have about the mass of the Sun. Thus white dwarf are very compact, dense objects. The Pauli exclusion principle requires the free electrons to have different energy levels. This requirement of higher energy quantum states (“degeneracy”) appears as a pressure that balances the force of gravity in the white dwarf and is largely

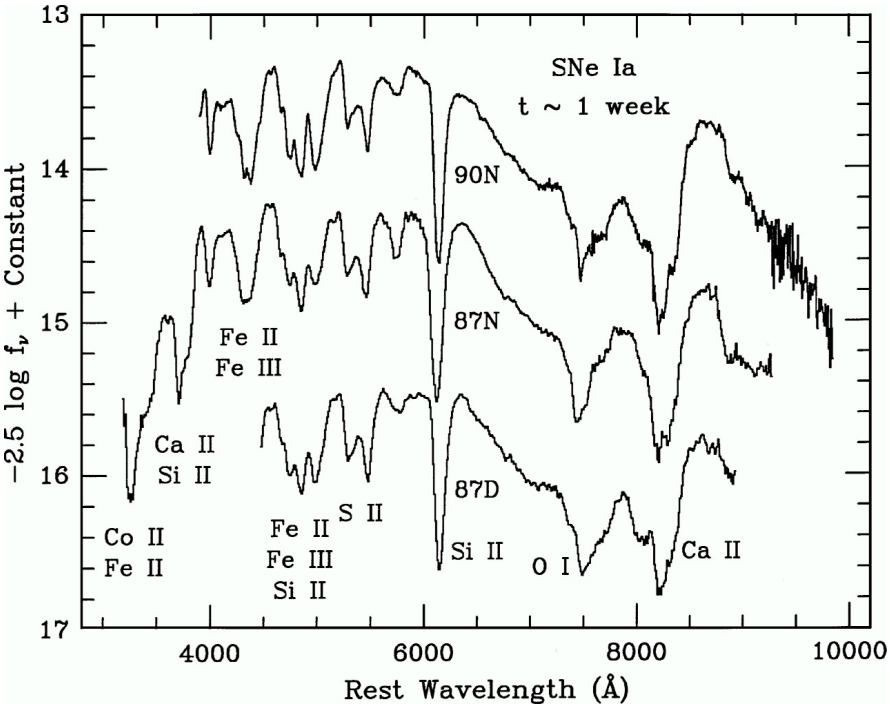

Figure 1.1: Remarkably similar spectra for three different supernovae about 1 week after peak light. Figure from Filippenko et al. (1992).

independent of the temperature. For a degenerate star, the more massive the star is, the smaller it is ($R \sim M^{-1/3}$), but there is a limit on the mass called the Chandrasekhar limit, which is about 1.4 solar masses (Chandrasekhar 1935). The equation for the limiting mass is given by $M_{limit} \approx N^2(\hbar c/G)^{3/2}$, where N is the number of electrons per unit mass, $\hbar$ is the reduced Planck constant, c is the speed of light, and G is the gravitational constant. As the Chandrasekhar limit is approached from the accretion of material from a companion star, additional physics besides degeneracy pressure and gravity comes into play, namely subsonic turbulence, nuclear burning, and electron capture. Under appropriate conditions, the near Chandrasekhar mass white dwarf may explode to produce a SNIa (Chandrasekhar 1984).

Although SNIa are not strictly "standard candles," they obey a relation that can "standardize" their light curves. This is called the Phillips relation, which states

that for SNIa light curves, “brighter equals broader.” In other words, the longer it takes the supernova to dim, the brighter it is (Phillips 1993). Fig. 1.2 shows a pair of graphs from the Supernova Cosmology Project (Perlmutter et al. 1999) displaying the Phillips relation. This is shown in the diagram on the left, with brightness on the y-axis and days on the x-axis. The supernova light curves near the bottom are dimmer and narrower, while those near the top are brighter and broader. Thus, brighter means broader. Brighter SNIa light curves are a result of hotter (and more ionized) debris, which is due to increased amounts of radioactive iron. This drives a higher opacity, which leads to a longer time for radiation to leak out, thus the curve is broader. If we then apply a stretch factor to the curves, they can be corrected such that they all fall along the same curve. This is shown in the right diagram, again with time on the x-axis and brightness on the y-axis. This ability to "standardize" SNIa light curves is what makes SNIa useful as distance indicators.

One way in which SNIa are used as distance indicators is in the Hubble diagram. The Hubble Space Telescope Cluster Supernova Survey has charted the expansion of the universe using SNIa. Fig. 1.3 shows the Hubble diagram for their data. Each point on the curve represents the observations of a single supernova. The x-axis is the redshift of the galaxy in which the supernova resides. This redshift is determined by comparing the spectral lines of the galaxy to spectral lines at rest to determine how fast the galaxy is moving away from us. The y-axis is the distance modulus of the supernova itself. The distance modulus ($\mu = m - M$) is the difference between the apparent magnitude m of the supernova and its absolute magnitude M. The distance modulus can be corrected for interstellar reddening by adding a reddening term to the distance equation. The line going through the points represents the best fit to the data based on current universe models, and each color represents a different survey. The shape of the fit can be described by the Friedmann Equation, which represents the expansion of the universe and is given by:

$$\frac{H^2(z)}{H_0^2} = \Omega_m(1+z)^3 + \Omega_k(1+z)^2 + \Omega_{DE} \times \exp\left[\int 3(1+w(z))d\ln(1+z)\right] \quad (1.1)$$

where H_0 is the current rate of expansion, Ω_m and Ω_{DE} are the matter and dark energy densities with respect to the critical density, $w(z)$ is the dark energy equation of state parameter, and $\Omega_k = 1 - \Omega_m - \Omega_{DE}$ is the spatial curvature of the universe. For the case where $w < -1/3$, which is indicated by the current model, the universe is undergoing accelerated expansion. The best fit to the data suggests $\Omega_{DE} = 0.729$, and suggests that the universe is undergoing accelerated expansion that can be explained by the presence of dark energy, which has negative pressure and accounts for 73% of the matter energy in the universe. That Ω_m and Ω_{DE} sum to unity is a consequence of a flat universe, which is supported by measurements of anisotropies in the cosmic microwave background (CMB) by the Wilkinson Microwave Anisotropy Probe (WMAP) (Spergel et al. 2003). The error bars in the Hubble diagram suggest an uncertainty in the luminosity distance value of about 10%. The current accepted value for H_0 is 74.3 $\pm$ 2.1 km s^{-1} Mpc^{-1} as measured by NASA's Spitzer Telescope. In the case that there are multiple populations represented in the Hubble diagram, identifying and removing outliners from the primary population would help reduce the scatter in Hubble digram. The broad goal in separating the populations is to reduce the scatter in the about diagram to $\sim 1\%$.

Although a Type Ia supernova progenitor has never been directly observed, supernovae spectra and light curves give clues about progenitor systems. Studies suggest that there could be two populations of SNIa, which are distinguished by their progenitors. The single-degenerate scenario involves one white dwarf accreting mass from a low-mass companion, while the double-degenerate scenario involves two white dwarfs merging from a Keplerian orbit. The two populations are distinguished by properties deduced from spectral signatures, including the amount of unburned carbon and the

silicon velocity structure. Wang & Han (2012) summarize recent observations to put constraints on SNIa progenitor systems. They conclude that white dwarf binary systems could, under some conditions, produce average SNIa, and that there is likely more than one progenitor responsible for the production of SNIa.

The most obvious outlying supernovae are removed from the sample used to make a Hubble diagram, but some of the less obvious ones could remain. These alternate progenitor supernovae could masquerade as "classical" Ia's, creating scatter in the Hubble diagram. To reduce the scatter in the Hubble diagram and improve calculations of cosmological parameters, more needs to be known about double-degenerate progenitors and how to distinguish them from single-degenerate progenitors. To that end, our goals for this project are to better understand the production of type Ia supernovae by double-degenerate mergers and to improve cosmological calibrations of SNIa. Specifically, from a stellar perspective we seek to know what systems contribute to the SNIa population. From a cosmological perspective, one way to decrease the scatter in the Hubble diagram is to homogenize the population used to make the diagram.

1.1 Previous Work

We are uncertain of what progenitor systems give rise to type Ia supernovae (Livio 2001). The single-degenerate scenario, involving a binary system containing a white dwarf and a low-mass star, have long been considered the predominant SNIa progenitors. In this paradigm, one option is that there are two main sequence stars in a binary orbit, one containing more mass than the other. The primary star evolves to the asymptotic giant branch first, and it's envelope expands. The primary star degenerates into a white dwarf, and the secondary star evolves into a red giant. The red giant star begins accreting mass onto the white dwarf, and the stars spiral in toward each other. When the white dwarf reaches the Chandrasekhar limit, a nuclear explosion or a collapse into

a neutron star ensues. In addition to a red giant, the white dwarf could accrete mass from a sub-giant or a main sequence star.

Although the single degenerate case has classically been favored, the single-degenerate scenario has trouble explaining how to grow the white dwarf to the Chandrasekhar limit, and the failure to observe hydrogen and helium from a low-mass companion. The double-degenerate scenario, on the other hand, involves two white dwarfs merging from a binary orbit and there are many arguments in favor of this scenario. These arguments include, but are not limited to: (1) double white dwarf binaries exist as a natural consequence of stellar evolution; (2) they provide an easy way to approach a critical mass; (3) they naturally explain the absence of hydrogen and helium in SNIa spectra; (4) they provide a logical explanation for the SNIa rate as a function of galaxy type; (5) population synthesis models have long predicted about the right frequency for double-degenerate systems to significantly contribute to the overall SNIa population.

Observationally, several white dwarf binaries have been found that will merge within a Hubble time (Napiwotzki et al. 2007). This model has not been favored in the past because previous simulations have yielded temperatures at the core-envelope interface too high to produce a Type Ia supernova (Livio 2000). However, the introduction of rotation could produce a more extended envelope, thereby reducing the interface temperature.

Although SNIa light curves vary, their variations are typically due to distance-independent parameters, such as the decline from B band maximum after 15 days (Phillips 1993). Using standard template calibrations, SNIa distance indicators are accurate to $\sim$10% (e.g., Silverman et al. 2012) and are primarily applied to "normal" SNIa (Branch et al. 1993). These "normal" SNIa are assumed to emerge from a homogeneous population of white dwarf progenitors. Observations of SN 2011fe in the galaxy M101 indicate the possibility of an alternate progenitor system (Nugent et al.

2011a). At a distance of 6.4 Mpc, the exploding star of SN 2011fe was likely a carbon-oxygen white dwarf. Due to the lack of an early shock, the companion was probably a main-sequence star. From pre-explosion images, a luminous red giant and most helium stars are ruled out as progenitors (Nugent et al. 2011b).

Other efforts, including those involving in-spiraling white dwarf binaries, have focused on realism of initial conditions (Rasio & Shapiro 1995; Pakmor et al. 2010; Dan et al. 2011; Raskin et al. 2012), unequal mass collisions (Benz et al. 1989, 1990; Rosswog et al. 2009; Lorén-Aguilar et al. 2010; Raskin et al. 2010; Pakmor et al. 2012), and the final long-term fate of merged systems (van Kerkwijk et al. 2010; Yoon et al. 2007; Shen et al. 2012). In contrast, our simulations are idealized, and highlight the essential physics and numerical convergence properties of the simplest possible configuration. These idealized simulations form a baseline for further studies that incorporate more realistic initial conditions.

A double-degenerate merger model has been presented by Yoon et al. (2007). This model shows the evolution of a double-degenerate system during the merging process. The two stars in the model are 0.6 and 0.9 solar masses, making the total mass of the system exceed the Chandrasekhar limit. They find that, with certain conditions met (maximum temperature, minimum angular momentum loss time-scale, and maximum mass accretion rate), double-degenerates are good progenitor candidates.

A study by Dan et al. (2012) considers white dwarfs with masses from 0.2 to 1.2 $M_\odot$ with different chemical compositions. Fig. 1.4 shows the parameter space of mergers when the system first crosses. The x-axis is M_1 and the y-axis is M_2, ranging from 0.4 to about 1.1 $M_\odot$ each. The colorbar represents density, with blue being the sparsest and yellow the densest. They split the diagram into two regions, He-donors below 0.6 $M_\odot$ and CO-donors above 0.6 $M_\odot$ for M_2. Mergers that are near equal mass produce symmetric, coalesced objects at the time shown, while highly unequal mass

mergers produce one object accreting mass from the other. They find that a supernova progenitor can come from variety of dynamically unstable white dwarf merger systems, and they find little evidence for explosion prior to the merger in carbon-oxygen systems.

Raskin et al. (2010) perform a similar exploration of parameter space. Fig. 1.5 shows 2D density images of a 3D projection of the white dwarf collision at different points in time, from 20 seconds after the simulation start to 100 seconds after. The arrows indicate the velocity vector of the stars at first contact. The stars orbit around each other, and begin to transfer mass between them, finally coalescing into one object. This study is amongst others that include, but arenâĂŹt limited to in-spiraling from a binary orbit, unequal mass collisions, and the final long-term fate of merged systems.

1.2 FLASH

We use FLASH, a parallel, Eulerian grid-based code with adaptive mesh refinement (AMR) and built-in self-gravity and nuclear burning. Fig. 1.6 illustrates adaptive mesh refinement in FLASH (Fryxell et al. 2000), showing a set of blocks where each block is outlined in bold. Each block has 8x8 cells, and the more refined regions have cells that are smaller by a factor of two. Below the blocks, there is a diagram of the tree structure and the block positions. At each step, the blocks can be refined or derefined as necessary, in order to modify the grid based on changes in density. FLASH can be used in two capacities: to investigate the global overview of the merger and to use AMR as a microscope to look at specific areas. Most previous studies of double-degenerate mergers were carried out using smooth particle hydrodynamics (SPH) codes. Additionally, our work is different from previous studies because we are going to use more spatial resolution and improved physics (an improved equation of state). We use an electron-positron equation of state based on table interpolation of the Helmholtz free energy (Timmes & Swesty 2000).

1.3 Physics of White Dwarfs

White dwarfs are composed of very dense degenerate matter, with a mass comparable to the Sun and a radius comparable to the Earth. When a white dwarf reaches the Chandrasekhar limit ($\approx 1.4 M_{\odot}$), the gravitational force exceeds the outward pressure force and the star will collapse. We use a 1D white dwarf model with the Helmholtz equation of state, then we map the 1D model onto the 3D grid. Hydrostatic equilibrium is assumed, given by Eqns. 1.2 and 1.3. Eqn. 1.3 is the Tolman-Oppenheimer-Volkoff (TOV) equation, which includes general relativistic effects. Without general relativity, the equation would simplify to Eqn 1.4. Eqn. 1.2 is the mass equation.

$$\frac{dM(r)}{dr} = 4\pi\rho(r)r^2 \tag{1.2}$$

$$\frac{dP(r)}{dr} = -\rho(r)\frac{GM(r)}{r^2}\left(1+\frac{P(r)}{\rho(r)c^2}\right)\frac{1+\frac{4\pi P(r)r^3}{M(r)c^2}}{1+\frac{2GM(r)}{rc^2}} \tag{1.3}$$

$$\frac{dP(r)}{dr} = -\rho(r)\frac{GM(r)}{r^2} \tag{1.4}$$

Fig. 1.7 shows the result of integrating the two first two equations above. Each line represents an integration for a different central density between 10^4 and 10^{11} g cm^{-3}. The point where each line crosses the x-axis indicates the total mass for each central density.

Fig. 1.8 shows the total mass (the x-axis intercept from Fig. 1.7 versus the central density. The relation is given for the $n = 3$ and $n = 3/2$ polytropes and for an Ideal Fermi Gas. The polytropic equation of state is $P = K\rho^{(n+1)/n}$, where K is a constant. In the low central density limit, the Fermi Gas approaches the $n = 3/2$ polytrope, and in the high central density limit it approaches the $n = 3$ polytrope. The polytropes provide a good first estimate, but the Ideal Fermi Gas is more realistic. The ideal Fermi

gas equation of state is given by $P = (1/40)(3/\pi)^{2/3}(h^2 n_e^{5/3}/m_e)$ for a fully degenerate non-relativistic system and $P = (1/16)(3/\pi)^{1/3} hcn_e^{4/3}$ for a fully degenerate relativistic system. As the diagram shows, general relativity terms do not have much of an effect, so we do not include them in our FLASH simulations.

1.4 Current Work

Our models start in FLASH with two white dwarfs, each of which is in hydrostatic equilibrium, and evolve through the dynamical phase of the merger to the quasi-equilibrium phase (a slowly-changing equilibrium where material is still falling in on the central object). By comparing our model results to observations, we can learn more about what distinguishes supernovae with double-degenerate progenitors. Features from spectra, like those shown in Fig. 1.1, can be compared to expected values from the model. We can find the total mass of the merged system, which will give an upper limit on the amount of observed ^{56}Ni. From the simulations, we will be able to determine the density structure of the quasi-equilibrium merged white dwarf system. The density structure determines the degree of compression of the layers responsible for producing silicon-group elements. This will place restrictions on the range of silicon velocity structures we see. Also, the density structure will place constraints on the region where carbon can burn into intermediate-mass elements. This will affect the amount of unburned carbon we observe (Filippenko et al. 1992). Using the results of our model and the observational constraints determined from the density structure, we will have further insight into the evolution of double-degenerate progenitors of SNIa. Understanding the progenitor systems of type Ia supernovae will allow us to improve cosmological calculations involving supernovae, leading to a better estimate of dark energy effects in cosmology.

To that end, I seek to answer the following questions in this dissertation: 1) Do collisions produce enough ^{56}Ni to make them supernova progenitor candidates? 2) Are

there other observational signatures besides ^{56}Ni to which we can direct our attention? 3) What parameters determine yields from mergers? 4) Are current results robust with respect to spatial resolution in literature?

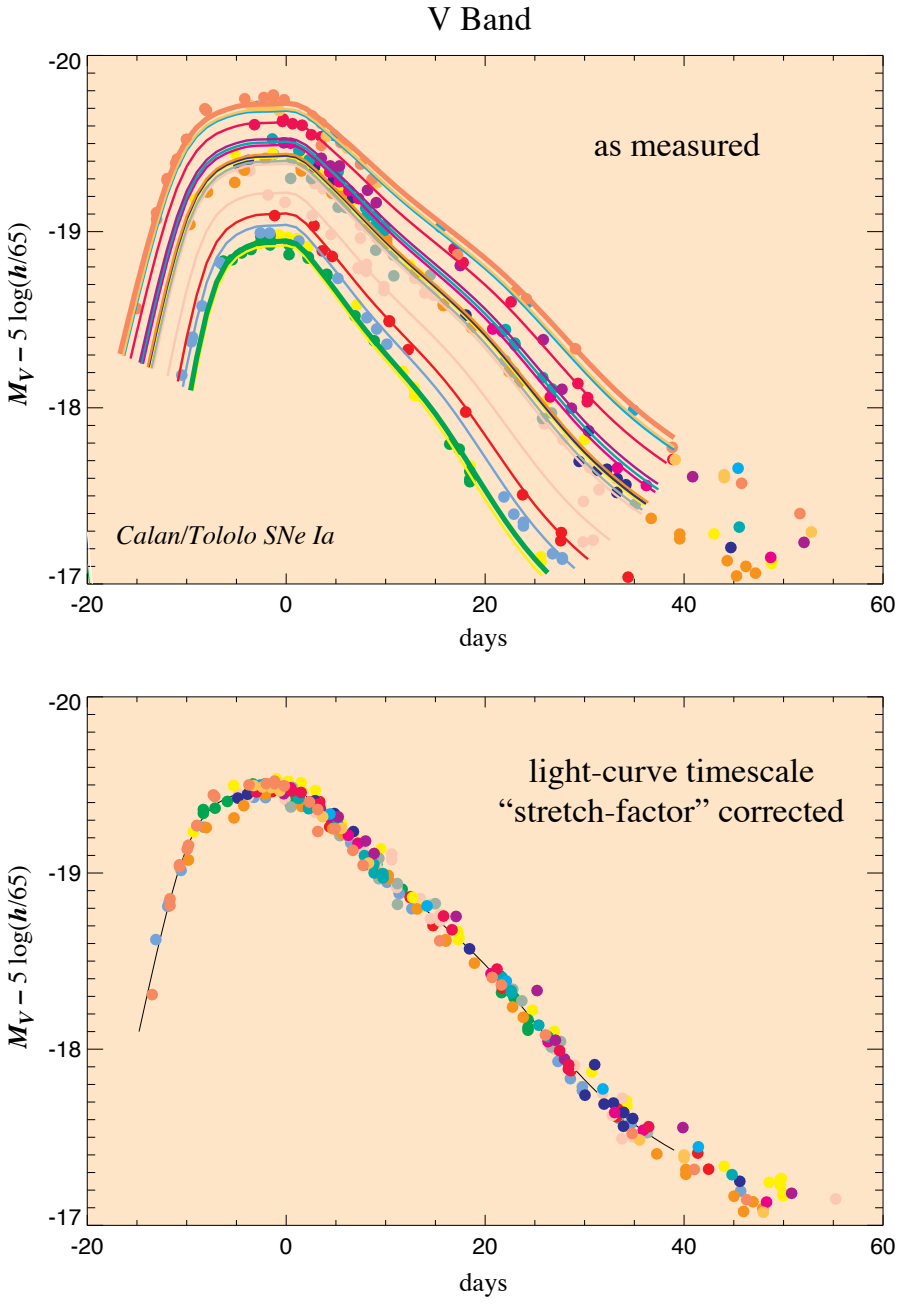

Figure 1.2: Plots showing the Phillips relation from Supernova Cosmology Project data. The brighter the supernova, the broader the light curve (left). However, a stretch factor can be used to standardize the curves (right).

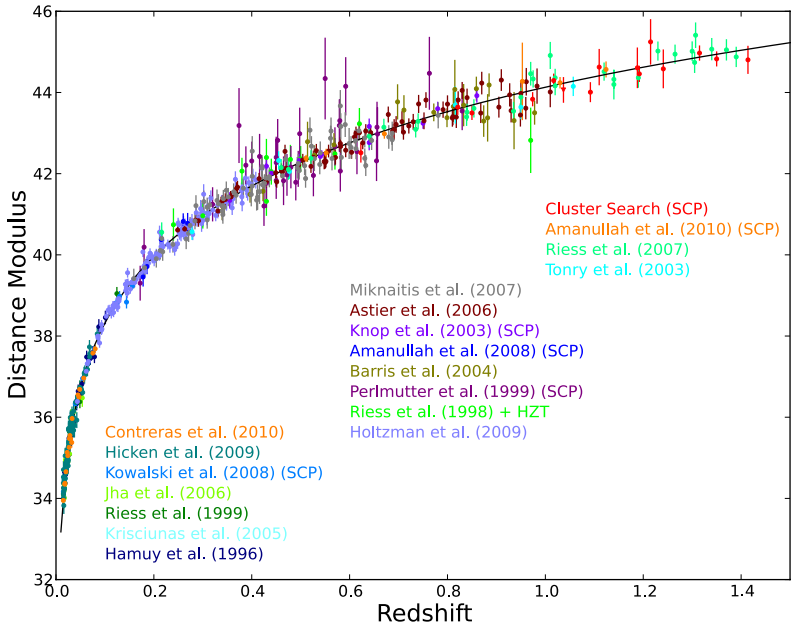

Figure 1.3: Hubble Diagram showing distance modulus versus redshift from Suzuki et al. (2012). The colors represent different surveys and the curve is the best fit to the current data. The shape of the fit can be described by the Friedmann Equation (Eqn. 1.1), which represents the expansion of the universe.

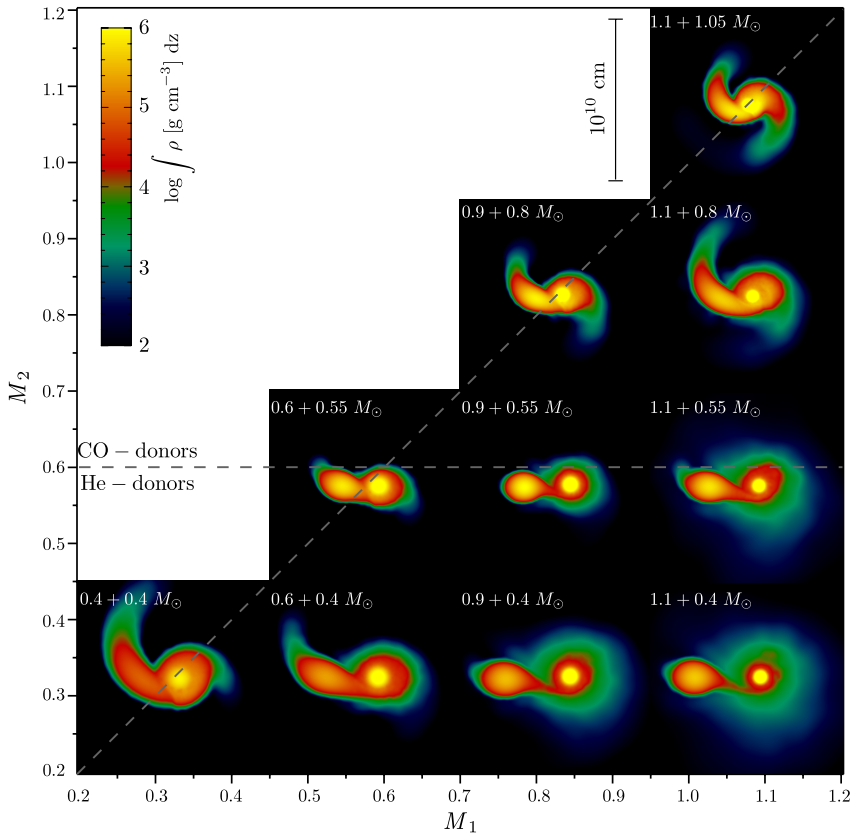

Figure 1.4: Figure from Dan et al. (2012) showing the parameter space of two white dwarfs merging when the stars are at first contact. This happens at different simulation times depending on the configuration. Each axis represents the mass (in solar masses) of each star in the system. The y-axis has a demarkation between He donors and CO donors at 0.6 solar masses. The colorbar corresponds to an integral of density with respect to z. For stars of approximately equal mass, the system is mostly symmetrical at first contact, and the stars are starting to form a single object. In systems where the mass of one star is much greater than the other, a system has formed where one star is accreting on to the other, and a single object has not formed.

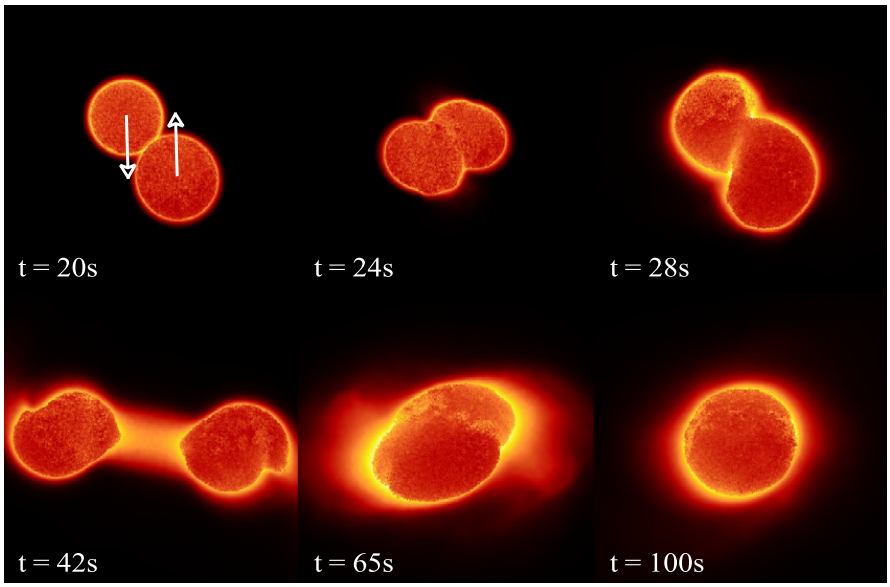

Figure 1.5: Figure from Raskin et al. (2010) showing a b=2 white dwarf collision from 20 seconds (first contact) to 100 seconds. The mass pairing is 0.64+0.64 solar masses. The arrows indicate the velocity vectors of the stars at first contact. Within the period of time shown, the white dwarfs exchange mass and coalesce into a single object. At 24 seconds the appear as though the have formed a single object, but at 28 seconds it is apparent that they are starting to move away from each other. At 42 seconds a mass exchange is seen between the two distinct objects, which then come back together by 65 seconds. At 100 seconds a single object has formed.

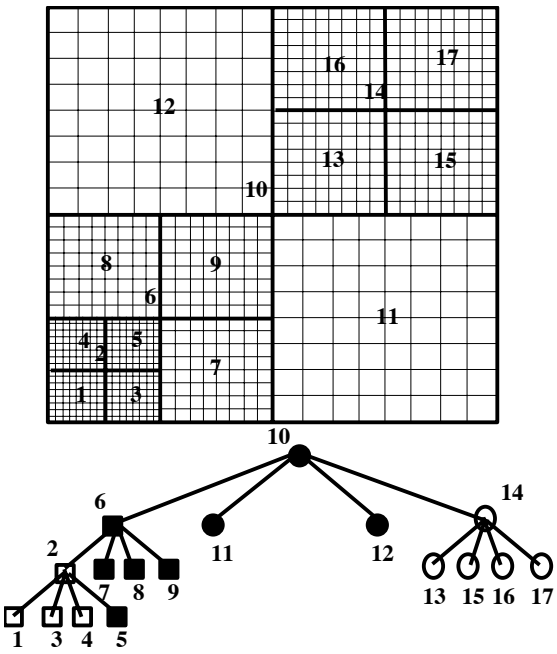

Figure 1.6: Figure from Fryxell et al. (2000) showing blocks in FLASH. Each block is outlined in bold, and contains 8x8 cells (the smaller boxes that are not in bold). For each increasing level of refinement, the boxes are further decreased by a factor of 2 in size in each dimension to allow more detail in regions with a higher change in density. Although refined blocks are smaller than their parent blocks, all blocks contain 8x8 cells. Different node types are attributed to a block. Node type 1 blocks are leaf nodes. The data of leaf nodes will always be valid. Leaf blocks have data which are used for plotting. This two dimensional structure is expanded into three dimensions in our simulations (each block is a cube with 8x8x8 cells.

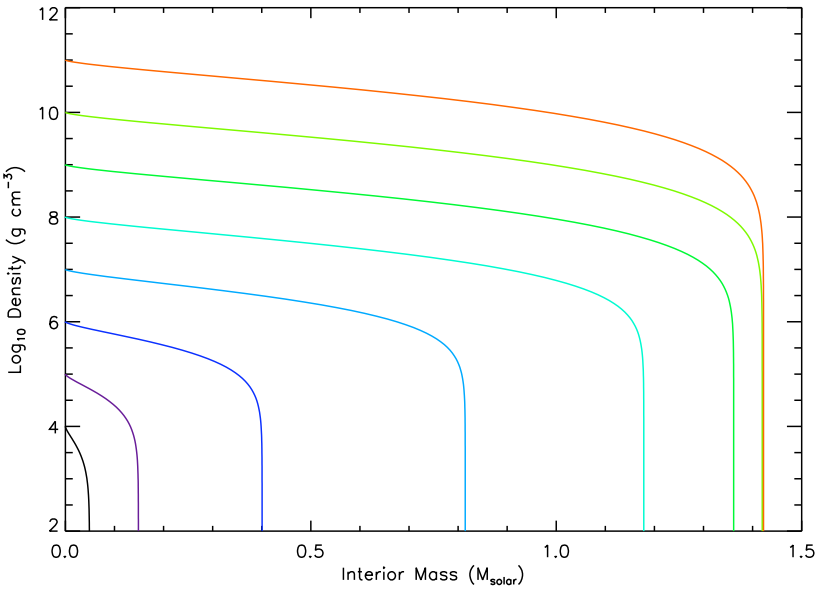

Figure 1.7: Density vs. interior mass for a cold (completely degenerate) white dwarf. Each line (and individual color) represents a different total mass. The total mass is shown by where the line hits the x-axis.For example, a white dwarf with a central density of 10^6 g cm^{-3} has a total mass of 0.4 solar masses (dark blue line).

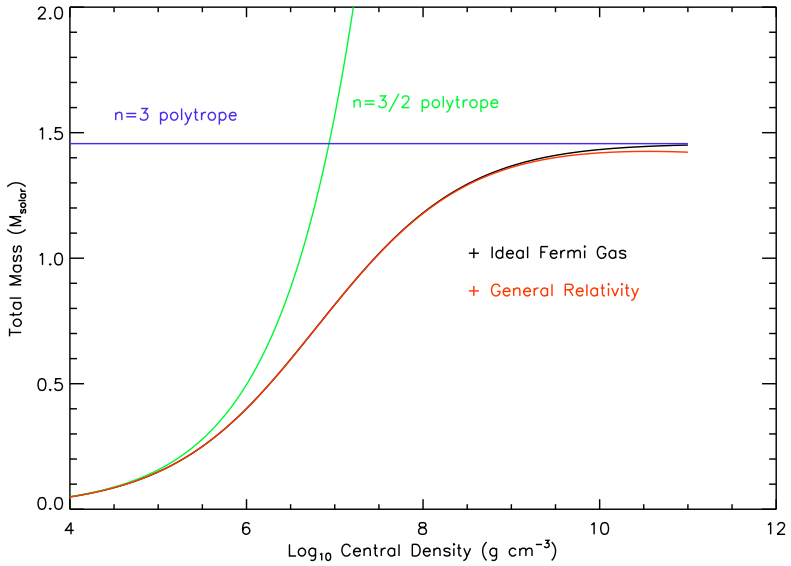

Figure 1.8: Total mass vs. central density for a cold (perfectly degenerate) white dwarf. The lines represent the n=3 polytrope (at the Chandrasekhar mass), the n=3/2 polytrope, the ideal fermi gas, and contributions from general relativity. The n=3 polytrope has constant total mass for every central density, while the n=3/2 polytrope has increasing mass for increasing central density. The ideal Fermi gas starts out approximately the same as the n=3/2 polytrope, but approaches the n=3 polytrope at high central density. The contributions from general relativity are relatively small.

Chapter 2

ZERO IMPACT PARAMETER WHITE DWARF COLLISIONS IN FLASH

Abstract

We systematically explore zero impact parameter collisions of white dwarfs with the Eulerian adaptive grid code FLASH for 0.64+0.64 $M_\odot$ and 0.81+0.81 $M_\odot$ mass pairings. Our models span a range of effective linear spatial resolutions from 5.2×10^7 to 1.2×10^7 cm. However, even the highest resolution models do not quite achieve strict numerical convergence, due to the challenge of properly resolving small-scale burning and energy transport. The lack of strict numerical convergence from these idealized configurations suggest that quantitative predictions of the ejected elemental abundances that are generated by binary white dwarf collision and merger simulations should be viewed with caution. Nevertheless, the convergence trends do allow some patterns to be discerned. We find that the 0.64+0.64 $M_\odot$ head-on collision model produces 0.32 $M_\odot$ of ^{56}Ni and 0.38 $M_\odot$ of ^{28}Si, while the 0.81+0.81 $M_\odot$ head-on collision model produces 0.39 $M_\odot$ of ^{56}Ni and 0.55 $M_\odot$ of ^{28}Si at the highest spatial resolutions. Both mass pairings produce $\sim$0.2 $M_\odot$ of unburned ^{12}C+^{16}O. We also find the 0.64+0.64 $M_\odot$ head-on collision begins carbon burning in the central region of the stalled shock between the two white dwarfs, while the more energetic 0.81+0.81 $M_\odot$ head-on collision raises the initial post-shock temperature enough to burn the entire stalled shock region to nuclear statistical equilibrium.

2.1 Introduction

Supernova Type Ia (SNIa) have continued to be foremost probes of the universe's accelerating expansion (Riess et al. 1998; Perlmutter et al. 1999; Riess et al. 2011; Sullivan et al. 2011; Suzuki et al. 2012). While light curves between different SNIa vary, the

variations generally correlate with distance independent light-curve properties, such as the decline from B band maximum after 15 days (Phillips 1993). Calibration of the light curves onto a standard template yields distance indicators accurate to $\sim$10% (e.g., Silverman et al. 2012) and are primarily applied to SNIa not showing peculiarities (Branch et al. 1993). These "normal" SNIa presumably emerge from a homogeneous population of white dwarf progenitors. While the favored population is thought to be a carbon-oxygen white dwarf (WD) accreting matter from a non-degenerate companion star (e.g., Whelan & Iben 1973; Thielemann et al. 1986), recent observations suggest that a fraction of SNIa may derive from double-degenerate progenitors (Howell et al. 2006; Hicken et al. 2007; Gilfanov & Bogdán 2010; Bianco et al. 2011).

In view of these and other observations of SNIa progenitor systems, recent theoretical studies have explored double degenerate mergers and collisions of white dwarfs as potential progenitors of SNIa (Guerrero et al. 2004; Yoon et al. 2007; Maoz 2008; Lorén-Aguilar et al. 2009; Raskin et al. 2009; Rosswog et al. 2009; Lorén-Aguilar et al. 2010; Pakmor et al. 2010; Raskin et al. 2010; Shen et al. 2012; Pakmor et al. 2012). Almost all of these efforts use smooth particle hydrodynamic (SPH) codes to model most of the collision or merger process. SPH and Eulerian grid codes, such as FLASH (Fryxell et al. 2000), have well-known complimentary strengths and weaknesses – particle codes are inherently better at angular momentum conservation, whereas grid codes have a superior treatment of shocks. Only Rosswog et al. (2009) included a zero impact parameter white dwarf collision model with FLASH. They used a mirror gravitational potential for one white dwarf at one spatial resolution. They found their FLASH calculations yielded about half as much ^{56}Ni as the equivalent SPH calculation (0.32 $M_\odot$ for SPH, 0.16 $M_\odot$ for FLASH).

In this paper, we use the Eulerian adaptive mesh refinement code FLASH to model the zero impact collisions between 0.64+0.64 $M_\odot$ and 0.81+0.81 $M_\odot$ carbon-

oxygen white dwarf mass pairings. Like the single case studied by Rosswog et al. (2009), our configurations are highly idealized cases of head-on collisions between identical, initially spherical white dwarfs. One aim of our paper is to determine whether or not, given presently available computing resources and numerical algorithms, simulations of collisions can be used to reliably predict the fraction of white dwarf material that is converted by explosive nucleosynthesis into heavier elements such as silicon and nickel. Other efforts have focused on the realism of the initial conditions and subsequent evolution, including but limited to, in-spiraling from a binary orbit (Rasio & Shapiro 1995; Pakmor et al. 2010; Dan et al. 2011; Raskin et al. 2012), unequal mass collisions (Benz et al. 1989, 1990; Rosswog et al. 2009; Lorén-Aguilar et al. 2010; Raskin et al. 2010; Pakmor et al. 2012), and the final long-term fate of merged systems (van Kerkwijk et al. 2010; Yoon et al. 2007; Shen et al. 2012). Our simulations, through their idealized nature, highlight the essential physics and numerical convergence properties of the simplest possible configuration. In addition, our idealized configurations form a baseline for further studies that incorprate more realistic initial conditions.

Our paper is organized as follows. In §3.2, we describe the input physics, initial conditions, and boundary conditions of our FLASH simulations. In §2.3, we discuss the results of our studies over a range of spatial resolutions and time-step choices, and in §2.4 we explore the implications of our results and describe directions for future studies.

2.2 Input Physics, Initial Conditions, and Boundary Conditions

Our 3D simulations are carried out with FLASH 3.2, a 3D Eulerian hydrodynamics code with adaptive mesh refinement (Fryxell et al. 2000; Calder et al. 2002). We use the included Helmholtz equation of state (Timmes & Swesty 2000), the 13 isotope alpha-chain reaction network that includes isotopes from ^{4}He to ^{56}Ni to model energy generation from nuclear burning (Timmes 1999), and the multigrid Poisson gravity

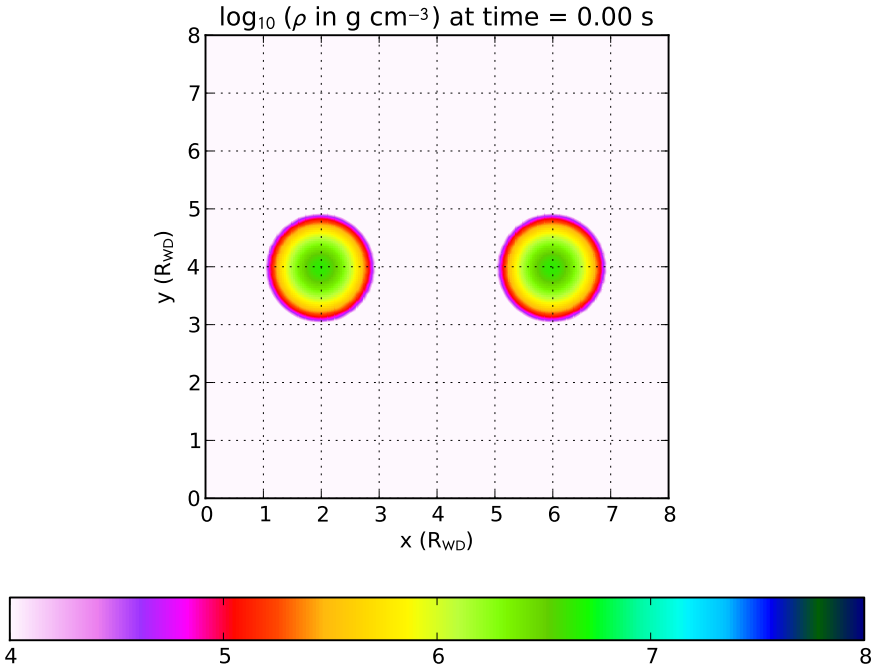

Figure 2.1: A 2D slice of density through the x-y mid-plane at t=0.0 s for the 0.64+0.64 $M_\odot$ collision. Each tick mark has a value of one white dwarf radius, which is 8.3×10^8 cm. The size of the domain is equal to eight white dwarf radii, and the white dwarfs are positioned four white dwarf radii apart from center to center.

solver with Dirichlet boundaries (Ricker 2008). All the simulation domain boundaries use a diode boundary condition, which is a zero-gradient boundary condition where fluid velocities are not allowed to point back into the domain. We follow both white dwarfs in 3D rectilinear coordinates throughout calculation, rather than using a mirror gravitational potential and evolving one white dwarf (as used in Rosswog et al. 2009).

Our initial 1D white dwarf profiles are calculated assuming hydrostatic equilibrium and mass conservation[1]. Our initial white dwarf models use the same equation of state as in FLASH, namely, the Helmholtz equation of state. We assume a uniform

[1]Code avaliable from http://cococubed.asu.edu/code_pages/coldwd.shtml

composition of 50% ^{12}C and 50% ^{16}O. We use white dwarfs with masses 0.64 and 0.81 $M_{\odot}$, to match the masses used in Raskin et al. (2010), with an isothermal temperature of 10^7 K. We map the 1D white dwarf profiles for the density, temperature and composition onto a 3D rectilinear Cartesian grid. Our computational domain is a cubic box chosen to be eight times the white dwarf radius (see Fig. 3.1). The white dwarfs are initially placed four white dwarf radii apart from center to center, which is large enough to allow the subsequent evolution to produce tidal distortions while allowing sufficient numerical resolution in the central regions.

The symmetry of head-on collisions between identical, initially spherical white dwarfs suggests 2D axisymmetric simulations may have been sufficient. Our rationale for deploying 3D rectilinear coordinates is three-fold. First, we want to explicitly show that FLASH maintains symmetry throughout the collision and subsequent explosion processes. Second, we want to compare our results on this important numerical test case with other existing 3D calculations (both grid and particle). Imposing axisymmetric conditions would have complicated these comparisons because we would not know if differences from existing 3D models were driven by different physics, different numerics or the imposition of axisymmetry itself. Third, we anticipate exploring unequal mass and non-zero impact parameter collision models with FLASH, both of which violate axisymmetry. To better assess the impact of these effects requires an equal mass, zero impact parameter, 3D benchmark calculation.

We use the free-fall expression for the initial, relative speed of the two white dwarfs, $v = [2G(M_1 + M_2)/\Delta r]^{1/2}$, where M_i are the masses of the constituent white dwarfs and Δr is the initial separation of their centers of mass, which for our initial conditions is $4R_{WD}$. Each white dwarf moves toward the other white dwarf, one in the positive x-direction and the other in the negative x-direction, with half of the relative

speed. The centers of both stars lie on the x-axis, and thus the initial velocities are purely in the x-direction.

The surrounding ambient medium is set to the same temperature as the isothermal white dwarfs with a density that is small (10^{-4} g cm^{-3}) compared to the density of the outermost regions of the white dwarf ($\sim$1-10 g cm^{-3}). Table 3.1 lists the initial conditions for each of our six simulations.

Table 2.1: Initial Conditions for the 3D FLASH models. Columns are the run number, white dwarf masses (M_1, M_2), maximum level of refinement (l), maximum spatial resolution (R), domain size (D), white dwarf initial velocities (v_1, v_2), the value of the timestep limiter (f), white dwarf radii ($R_{\rm WD}$), and central white dwarf densities ($\rho_{\rm WD}$).

#	M_1, M_2 ($M_\odot$)	l	R (10^7 cm)	D (10^9 cm)	v_1, v_2 (10^8 cm s^{-1})	f	$R_{\rm WD}$ (10^8 cm)	$\rho_{\rm WD}$ (10^6 g cm^{-3})
1	0.64	5	5.19	6.64	$\pm$1.59	0.2	8.30	4.51
2	0.64	6	2.59	6.64	$\pm$1.59	0.2	8.30	4.51
3	0.64	7	1.30	6.64	$\pm$1.59	0.2	8.30	4.51
4	0.81	5	4.32	5.51	$\pm$1.97	0.2	6.88	11.2
5	0.81	6	2.16	5.51	$\pm$1.97	0.3	6.88	11.2
6	0.81	7	1.08	5.51	$\pm$1.97	0.3	6.88	11.2

Our FLASH models begin with 1 top-level initial block, where each block contains 8 cells in each direction (x,y,z). The blocks are refined or derefined at each time-step based on changes in density and pressure. For each successive level of refinement, the block size decreases by a factor of two, creating a nested block structure. At maximum refinement, the smallest block size is determined by $R = D/(8 \times 2^{l-1})$, where D is the domain size in one dimension and l is the maximum level of refinement as seen in Table 3.1. At first contact between the white dwarfs, shock waves are sent into the ambient medium, causing the grid in the ambient medium to rapidly become maximally refined. To avoid concentrating resources on these less interesting regions of the models, we use a derefine procedure at first contact that sets a radius equal to 1.2 white dwarf radii beyond which the blocks in the ambient material are forced to be less refined than the blocks in the collision region.

The nuclear reaction network in FLASH uses constant thermodynamic conditions over the course of a timestep. However, the Courant limited hydrodynamic timestep may be so large compared to the burning timescale that the nuclear energy released in a cell may exceed the existing specific internal energy. To ensure the hydrodynamics and burning remain coupled, as well as to capture the strong temperature dependence of the nuclear reaction rates, we limit the timestep as a result of nuclear burning by a factor f, which constrains the maximum allowable change in specific internal energy. The overall timestep is $dt_{n+1} = \min[dt_{\rm hydro}, dt_{\rm burn}]$, where

$$dt_{\rm burn} = dt_n \times f \times \frac{u^i_{n-1}}{u^i_n - u^i_{n-1}} \ , \tag{2.1}$$

where the subscript n refers to the timestep number, $dt_{\rm hydro}$ is the hydrodynamic timestep, $dt_{\rm burn}$ is the burning timestep, and u^i is the specific internal energy of the ith cell. Table 3.1 lists the nominal values of f used for our six simulations, and the effects of using different values of f is discussed in §3.5.

2.3 Results

General Features of the Collision Models

Zero impact parameter, or head-on, white dwarf collisions undergo four distinct phases of evolution. First, the white dwarfs become tidally distorted as they approach each other. For the 0.64+0.64 $M_\odot$ case (hereafter 2×0.64), the velocity gradient across the white dwarf at first contact ranges from about 3500 km s^{-1} to 5000 km s^{-1}. Second, a shock wave is produced normal to the x-axis at first contact. The shock stalls because the speed of infalling material and the sound speed are comparable. Third, nuclear burning is initiated within the stalled shock region. Finally, the nuclear energy released unbinds the system, leading eventually to homologous expansion.

An overview of the evolution of the 2×0.64 collision is shown in Fig. 3.9. The 3D calculation has been sliced through the x-z mid-plane to show detail at the center

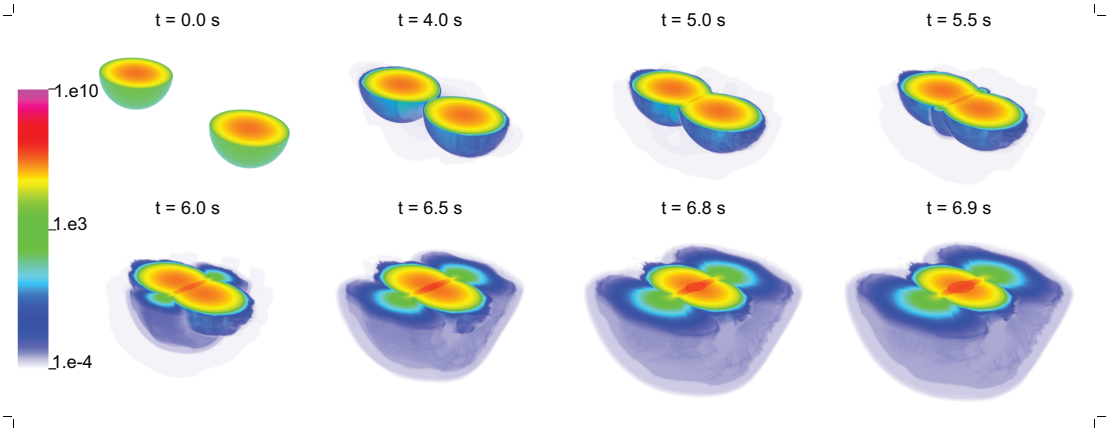

Figure 2.2: 3D images cut through the center of the y-axis of the 2×0.64 collision density from first contact at 0.0 s to after ignition at 6.9 s. For scale, each white dwarf has a radius of 8.3×10^8 cm. The density colorbar is logarithmic and extends from 10^{-4} to 10^{10} g cm^{-3}

.

of the collision. Due to the symmetry of a head-on collision, a cut through the x-z mid-plane will look identical to a cut through the x-y mid-plane. The top panel of the figure represents four times in the collision from the start of the simulation (t=0.0 s), to first contact (t=4.0 s), to the formation of the stalled shock region (t=5.0 s), and finally, to the jettisoning of material orthogonal to the x-axis (t=5.5 s).

Given the white dwarf radius and initial velocity shown in Table 3.1 for the 2×0.64 collision, the time to first contact would be $2R/v$=5.2 s if the initial speed was constant and the white dwarfs remained spherical. However, the initial speed increases due to gravitational acceleration and tidal distortion causes the white dwarfs to become elongated along the x-axis. As a result the two white dwarfs experience first contact sooner, at about 4.0 s.

The bottom panel represents the the further progression of the collision from the continued jettison of material (t=6.0 s), to just before ignition (6.5 s), to just after ignition (t=6.8 s), and finally to the spread of nuclear burning through the white dwarfs (t=6.9 s). These steps are discussed in further detail below.

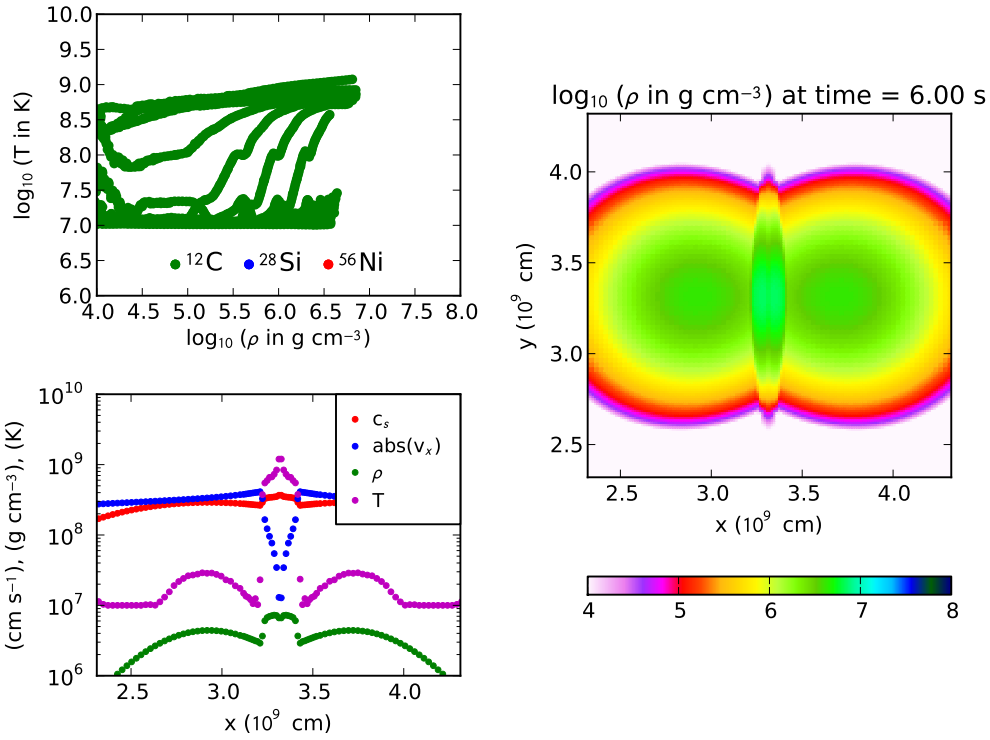

Figure 2.3: Analysis images of the 2×0.64 collision at t=6.00 s, after first contact, but before ignition. Top-left: Locations of all cells in the density-temperature plane. The color of the points represents the primary composition of the corresponding cell: green for ^{12}C, blue for ^{28}Si, and red for ^{56}Ni. The data are binned into 100 equally spaced bins in logarithmic density and temperature. Bottom-left: Temperature, x-velocity, density, and sound speed along the x-axis. Right: A 2D slice of density through the x-y mid-plane.

Fig. 3.4 shows the thermodynamic, mechanical, and morphological properties of the 2×0.64 head-on collision model. At 6.00 s after the beginning of the model, the white dwarfs are past first contact but have not yet begun runaway nuclear burning. The right panel shows the mass density profiles of a slice through the simulation in the x-y plane. In addition to the ambient medium (white in the figure), there are two distinct regions of density: the uncollided white dwarf material and the stalled shock region. The density and temperature are not yet high enough to fuel runaway burning. The lower left panel of Fig. 3.4 shows these quantities as well as the sound speed and velocity in

the x-direction along a line connecting the centers of the two white dwarfs and parallel to the x-axis. The sound speed is lower than the infall velocity speed, causing the stalling of the shock region. The temperature profile peaks at $\approx 10^9$ K, which is not hot enough to reach the carbon burning threshold. The upper left panel of Fig. 3.4 shows the state of the collision in the density-temperature plane. The color of the points represents the primary composition of the corresponding cell; green for ^{12}C, blue for ^{28}Si, and red for ^{56}Ni. Material with T$\approx 10^7$ K represents the cold and dense parts of the two stars that have not yet collided. The region with $10^7 < T < 10^9$ K and $10^4 < \rho < 10^{6.5}$ g cm^{-3}, represents the shocked material. At this point in the collision, "tracks" run from the lower left to the upper right, representing tori of material orthogonal to the x-axis at the center of the collision. In this case, ^{28}Si and ^{56}Ni have not yet been produced, thus all the cells are primarily composed of ^{12}C.

Fig. 3.5 has the same format as Fig. 3.4 at 6.60 s when runaway nuclear burning has begun. On the right panel, there are three distinct regions of the collision at this point in time: the white dwarf material which has not yet experienced the collision; the lenticular, nearly isobaric, stalled shock region; and the central region where a detonation has begun to propagate. The detonation front is outlined by the darker colored (higher density) oval region in Figs. 3.5. Our FLASH simulations do not resolve the initiation of the detonation. Instead, at all spatial resolutions investigated, the central-most cell in the 2×0.64 head-on collision model undergoes runaway carbon burning which begins to propagate a detonation.

In the lower left panel of Fig. 3.5, again, three distinct regions are visible - the unshocked white dwarfs the stalled shock, and the central-most detonation region. The temperature in the unshocked white dwarf material rises smoothly from the initially imposed background temperature of 1×10^7 K to $\approx 3 \times 10^7$ K at the centers of both white dwarfs because of low-amplitude velocity waves sloshing around the white dwarf

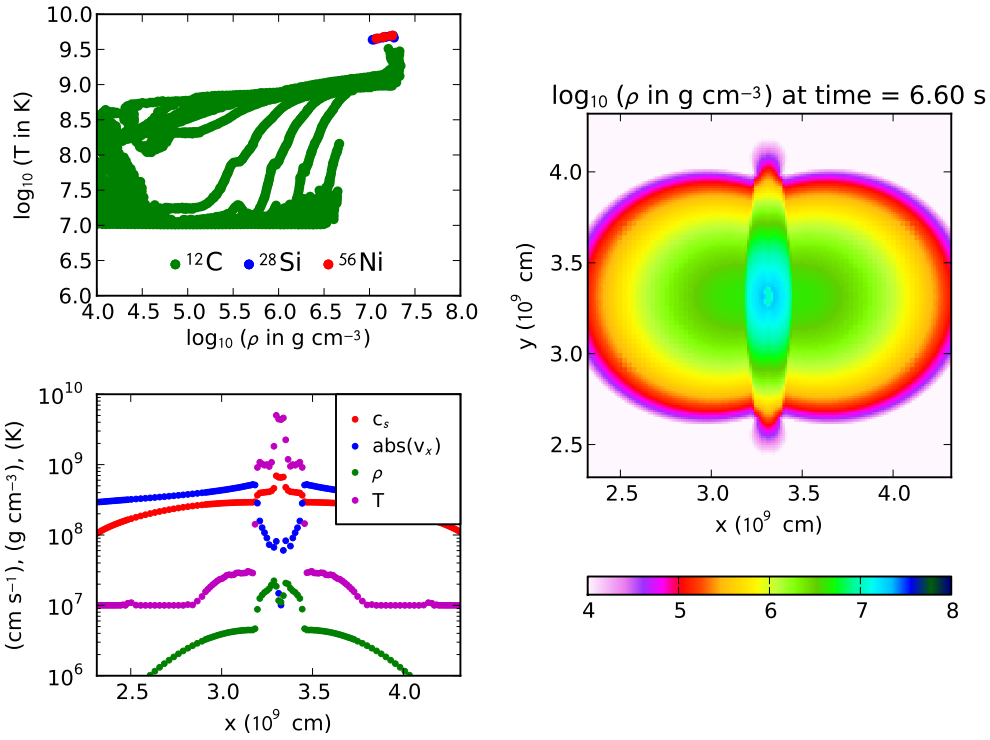

Figure 2.4: Same format as Fig. 3.4, when the model is at t=6.60 s, right after ignition.

interiors. However, 3×10^7 K is well below the carbon burning threshold, does not lift the electron degeneracy of the material, and does not impact our results. In the unshocked region, the infall speed of material is greater than the local sound speed. The material behind the stalled shock reaches temperatures that are sufficient to lift electron degeneracy and are just below the carbon burning threshold of $\approx2\times10^9$ K. The density in the stalled shock region reaches a peak of $\approx2\times10^7$ g cm^{-3}. In the innermost region where a detonation front has traveled $\sim 5\times10^7$ cm from the center, the temperature is $\approx6\times10^9$ K and the density dips to $\approx1\times10^7$ g cm^{-3}. In the upper left panel of Fig. 3.5, hot, dense material with T$>10^9$ K and $\rho>10^7$ g cm^{-3} from the central regions of the collision are in the upper right corner where the original carbon material has burned to ^{28}Si and ^{56}Ni.

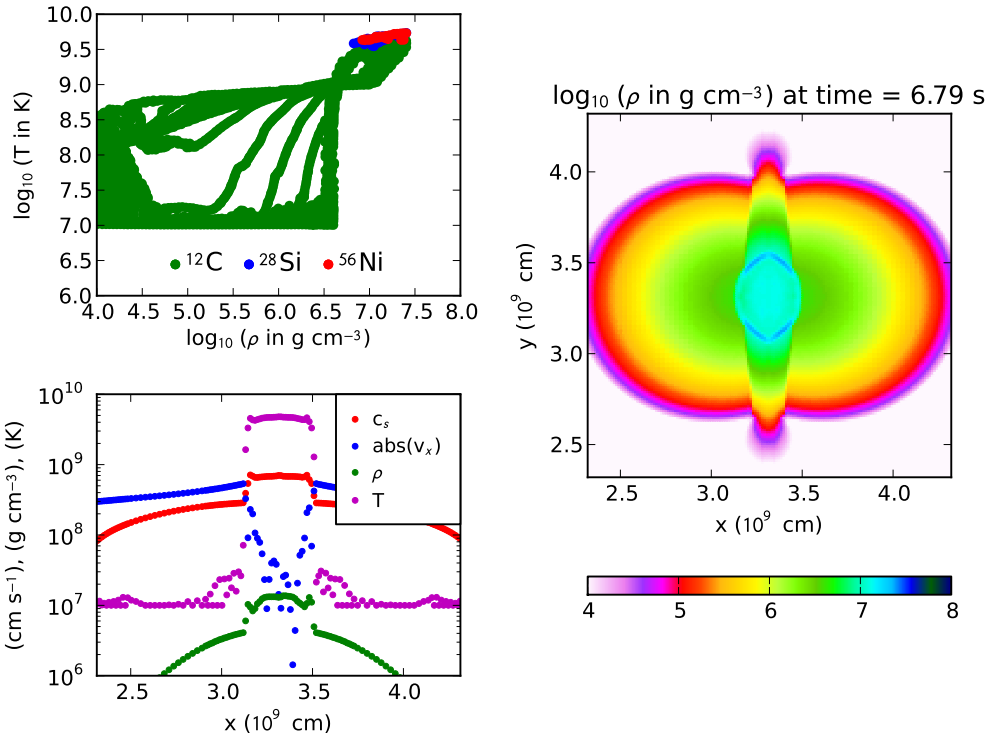

Figure 2.5: Same format as Fig. 3.4, when the model is at t=6.79 s, as the stalled shock region slightly expands and the densest parts of the white dwarfs begin to enter the stalled shock region.

Fig. 3.6 has the same format as Fig. 3.4 and the right panel shows the density profile when the detonation front has traveled outward from the center and the densest parts of the white dwarfs are about to enter the stalled shock region. The upper left panel indicates that more ^{12}C material is present in the high density regime with $\rho > 10^7$ g cm^{-3}, and being burned to ^{28}Si and ^{56}Ni. The lower left panel shows that the sound speed in the burned region is comparable with the speed of the infalling material, and the width of the detonation has expanded.

As additional energy from nuclear burning is added, the double white dwarf system eventually becomes gravitationally unbound. Fig. 3.7 has the same format as Fig. 3.5. The right panel shows the density distribution of the system slightly before

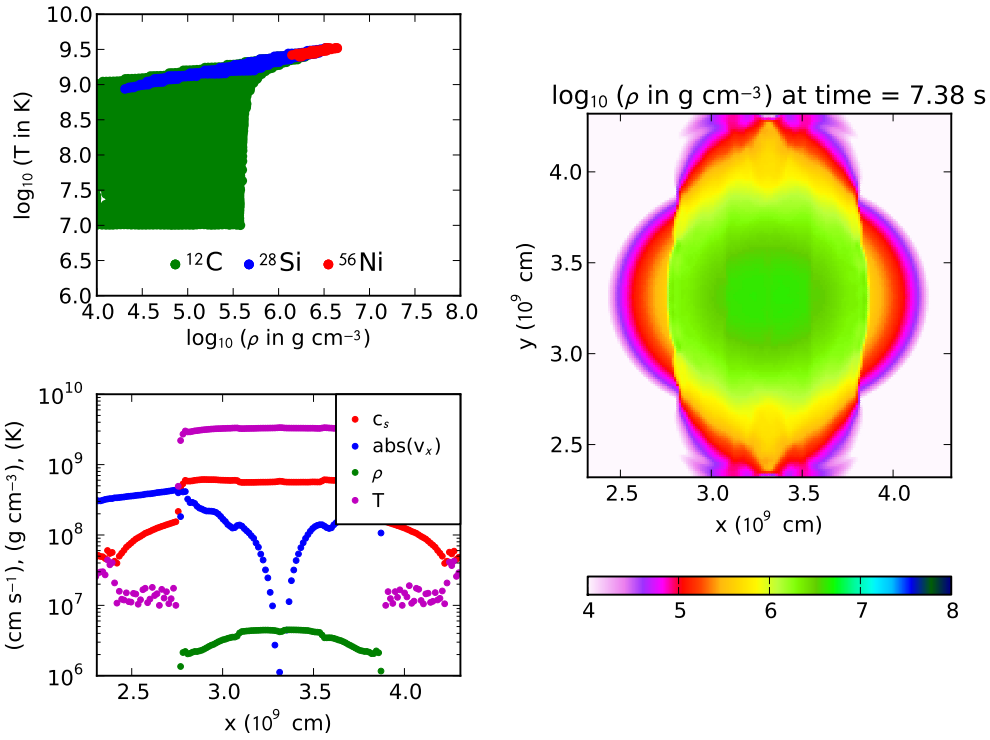

Figure 2.6: Same format as Fig. 3.4 at t=7.38 s, just before the system becomes gravitationally unbound.

the explosion reaches homologous expansion. The innermost 10^9 cm reaches a nearly constant temperature of $\approx 3\times10^9$ K with a slowly varying density distribution that peaks at $\approx 5\times10^6$ g cm^{-3}. The density-temperature plot in the upper left panel indicates larger amounts of high density, high temperature material with $\rho > 10^6$ g cm^{-3} and T$>10^9$ K. More material has achieved the conditions necessary to synthesize ^{28}Si (blue) and ^{56}Ni (red). the lower left panel shows the sound speed is always greater than the infall speed of the remaining material.

The 0.81-0.81 M$_\odot$ (hereafter 2×0.81) collision models evolve through a similar set of stages as the 2×0.64 collision models, except the larger kinetic energy at impact is sufficient for the initial shock to raise the temperature well above the ^{12}C+^{12}C

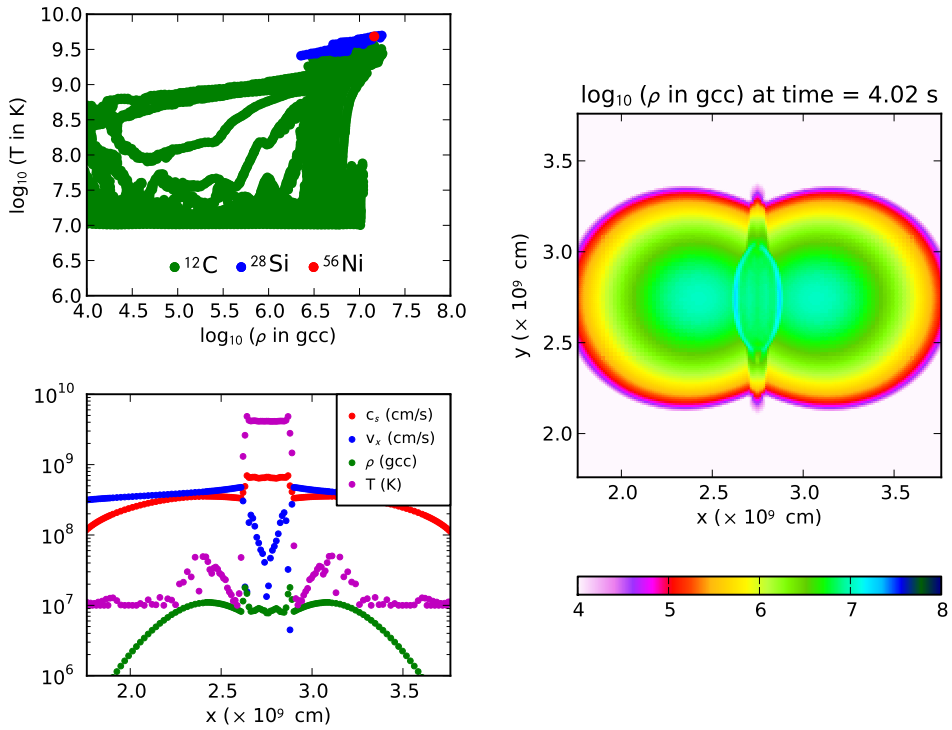

Figure 2.7: Same format as Fig. 3.4 at t=4.02 s for the 2×0.81 collision model.

threshold. Fig. 2.7 shows that the entire stalled shocked region burns rapidly to a state of nuclear statistical equilibrium and achieves a nearly isothermal state. Central ignition does not occur because the ^{12}C+^{16}O material has already been burned to nuclear statistical equilibrium. We discuss this difference in additional detail in §2.3.

Otherwise, the stages of the 2×0.81 collision are very similar to the evolution of the 2×0.64 collision seen above, with the 2×0.81 collision producing a greater amount of ^{56}Ni.

Numerical Convergence

To assess the numerical convergence, we performed the 2×0.64 and 2×0.81 simulations at three different spatial resolutions. Each increase in spatial resolution is a factor

of two more refined in one dimension, a factor of eight in volume (see Table 3.1), and takes at least twice as many time steps depending on the burning timestep. As the spatial resolution increases, the cells that are burning carbon to heavier elements become smaller in volume and the timestep decreases, leading to improved coupling between the hydrodynamics and nuclear burning.

Table 3.2 lists the ejected masses for each of the six convergence simulations and Fig. 2.8 shows the convergence behavior of ^{12}C+^{16}O, ^{28}Si, ^{56}Ni yields, as well as the internal energy, kinetic energy, and the total energy at the end of the simulation. The upper plot in Fig. 2.8 shows that for the 2×0.64 collision the ^{56}Ni mass (dashed red) increases, the ^{28}Si mass (dashed blue) decreases, and the ^{12}C+^{16}O (dashed green) decreases as the spatial resolution increases. The percent change in ^{56}Ni production is 138% between the $R = 5.19 \times 10^7$ cm and $R = 2.59 \times 10^7$ cm models, and 3.3% between the the $R = 2.59 \times 10^7$ cm and $R = 1.30 \times 10^7$ cm models. Although higher resolution models are needed to reach numerical convergence, the ^{56}Ni mass is approaching convergence at 0.32 $M_\odot$ (see Table 3.2). The internal energy (solid green) at the end of the 2×0.64 collision simulation decreases with increasing spatial resolution, but the kinetic energy (solid blue) when the model terminates increases with increasing spatial resolution. The net result is that the total energy (solid red) is nearly constant over the range of resolutions explored.

Table 2.2: Ejected Masses.

M_1, M_2 ($M_\odot$)	R (10^7 cm)	^{12}C + ^{16}O ($M_\odot$)	^{28}Si ($M_\odot$)	^{56}Ni ($M_\odot$)
0.64	5.19	0.29	0.45	0.13
0.64	2.59	0.21	0.37	0.31
0.64	1.30	0.19	0.37	0.32
0.81	4.32	0.19	0.41	0.62
0.81	2.16	0.19	0.50	0.45
0.81	1.08	0.18	0.53	0.39

The lower panel in Fig. 2.8 shows that for the 2×0.81 collision the ^{56}Ni mass decreases, the ^{28}Si mass increases as the spatial resolution increases, and the ^{12}C+^{16}O slightly decreases. Although convergence has not been achieved, the ^{56}Ni mass is approaching convergence at 0.39 $M_{\odot}$ (see Table 3.2). We discuss the reason for the different convergence trends between the 2×0.64 and 2×0.81 cases below. The internal energy and kinetic energy at the end of the 2×0.81 collision simulations appears to be oscillating towards convergence as the spatial resolution is increased. As a consequence of the internal energy and kinetic energy being out of phase, the total energy is nearly constant over the range of resolutions explored.

Although strict numerical convergence has not been achieved with these six simulations, some trends can be seen. As the total mass of the binary system increases in zero impact parameter collisions, the ^{56}Ni mass increases, indicating that larger mass collisions will produce more ^{56}Ni. For both mass pairs at highest resolution, ≈0.2 $M_{\odot}$ of unburned ^{12}C+^{16}O was ejected.

Higher numerical resolutions are desirable, but prohibitively expensive for this study, as our most resolved 3D models required at least 200,000 CPU hours per run. Simulations with higher spatial resolution are not possible in the context of the current study because doubling the grid resolution in a 3D simulation effectively increases the number of cells by a factor of $\approx 2^3$ and the number of timesteps by a factor of 2, meaning over an order-of-magnitude increase in computational time. Although these effects can be ameliorated somewhat by adopting more aggressive derefinement criteria, further restricting the computational domain size, or relaxing the timestep controller f, we expect that increasing the maximum resolution another factor of two (6.5×10^6 cm for the 2×0.64 models and 5.04×10^6 cm for the 2×0.81 models) would require ≈ 2 million CPU hours per run, which is beyond our capabilities here.

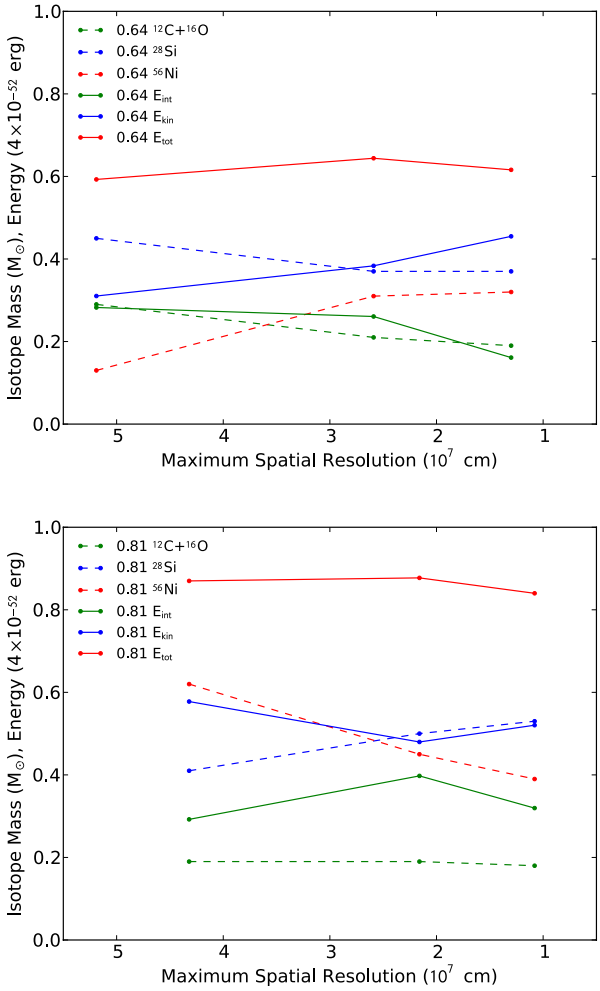

Figure 2.8: Convergence plot for the 2×0.64 (top) and 2×0.81 (bottom) head-on collisions. Points from left to right correspond to 5-, 6-, and 7-level runs for each collision. The dashed line colors represent different isotopes, where blue corresponds to ^{28}Si, green to ^{12}C+^{16}O, and red to ^{56}Ni. The solid line colors represent internal energy (green), kinetic energy (blue), and total energy (red).

Reducing the timestep limiting factor, f, and thereby reducing the timestep during nuclear burning changes the amount of ^{56}Ni produced. For example, changing from f=0.5 to f=0.1 in the 2×0.64 simulation with a spatial resolution of $R = 2.59 \times 10^7$ cm causes the ^{56}Ni production to increase by approximately 0.1 $M_\odot$, a 30% change. Fig. 2.9 shows the evolution of the hydrodynamic time step (solid lines), burning time step (dotted lines), and ^{56}Ni mass (dashed lines) for the 5-level (red), 6-level (green), and 7-level (blue) 2×0.81 collisions. We use f=0.2 for the 5-level run and f=0.3 for the 6- and 7-level runs to force the burning timestep to fall below the hydrodynamic timestep during the ^{56}Ni production phase. In all our simulations, we set f such that $dt_{burn} \approx 0.01 dt_{hydro}$ during the phase of evolution when nuclear burning is significant. Setting f to smaller values greatly increases the computing time without having a significant effect on the nucleosynthesis yields.

Fig. 2.8 shows that the 2×0.64 collision produces more ^{56}Ni as spatial resolution increases. To understand this behavior we examine profiles along the x-axis of the density and temperature for 5-, 6-, and 7-levels of refinement. The upper panel of Fig. 2.10 shows the three models with different spatial resolutions for the 2×0.64 collision at 5.6 s. The shocked region is widest in the 5-level model, and narrower in the 6- and 7-level models. The density is smaller (just below 3×10^6 g cm^{-3}) and nearly constant for the 5-level model, larger for the 6-level model than the 5-level model (3.5×10^6 g cm^{-3}), and slightly larger for the 7-level model than the 6-level model (3.6×10^6 g cm^{-3}). Both the 6- and 7-level models show a small valley in the central density. The peak temperature is smaller for the 5-level ($\approx 10^9$ K), and slightly higher for the 6-level and 7-level models (both above 10^9 K).

At 6.4 s (middle panel in Fig. 2.10), the density and temperature profile patterns as described for 5.6 s generally still hold, but the peak temperature is now the same for all three levels of refinement ($\approx 1.5 \times 10^9$ K). Detonation occurs just after this time

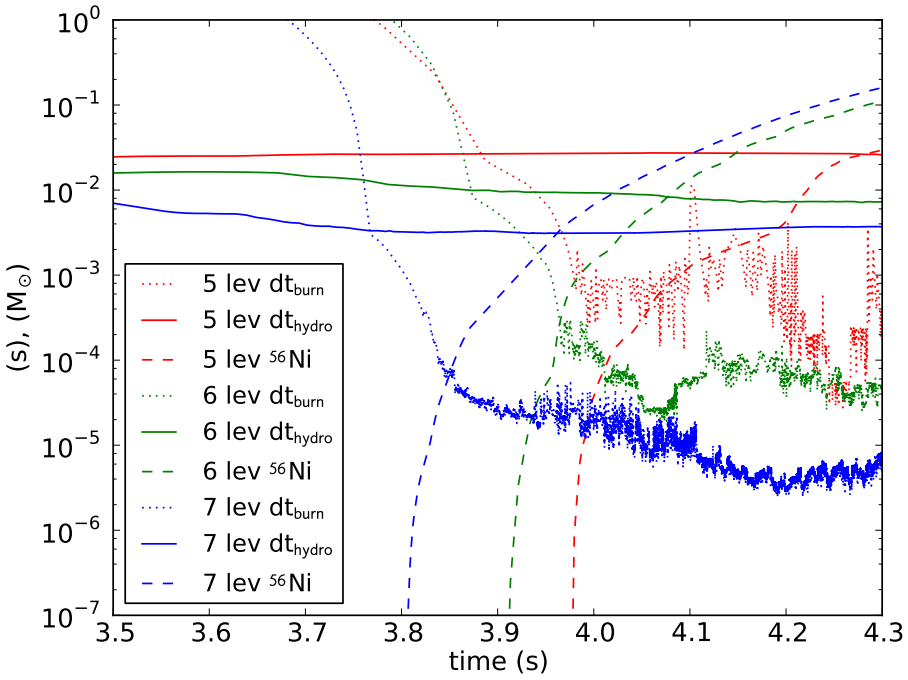

Figure 2.9: Evolution of the hydrodynamic time step (solid line), burning time step (dotted line), and ^{56}Ni mass (dashed line) for the 5-level (red), 6-level (green), and 7-level (blue) models of the 2×0.81 collision.

frame (as seen below). Thus, we expect to see more ^{56}Ni produced for the 6-level and 7-level models than for the 5-level model because there is more material in the shocked region with high density ($> 10^7$ g cm^{-3}) at the same ignition temperature. We also expect only a small difference in ^{56}Ni production between the 6- and 7-level models because the peak density is only slightly larger for the 7-level model and the width of the density profile is approximately the same. This explains the pattern in the the abundance yields with spatial resolution in Fig. 2.8.

At 6.9 s (lower panel in Fig. 2.10) when the detonation is underway, the Mach number is larger in the 7-level model than the 5- and 6-level models because the pre-detonation density is larger. This causes the 7-level temperature profile to be wider then

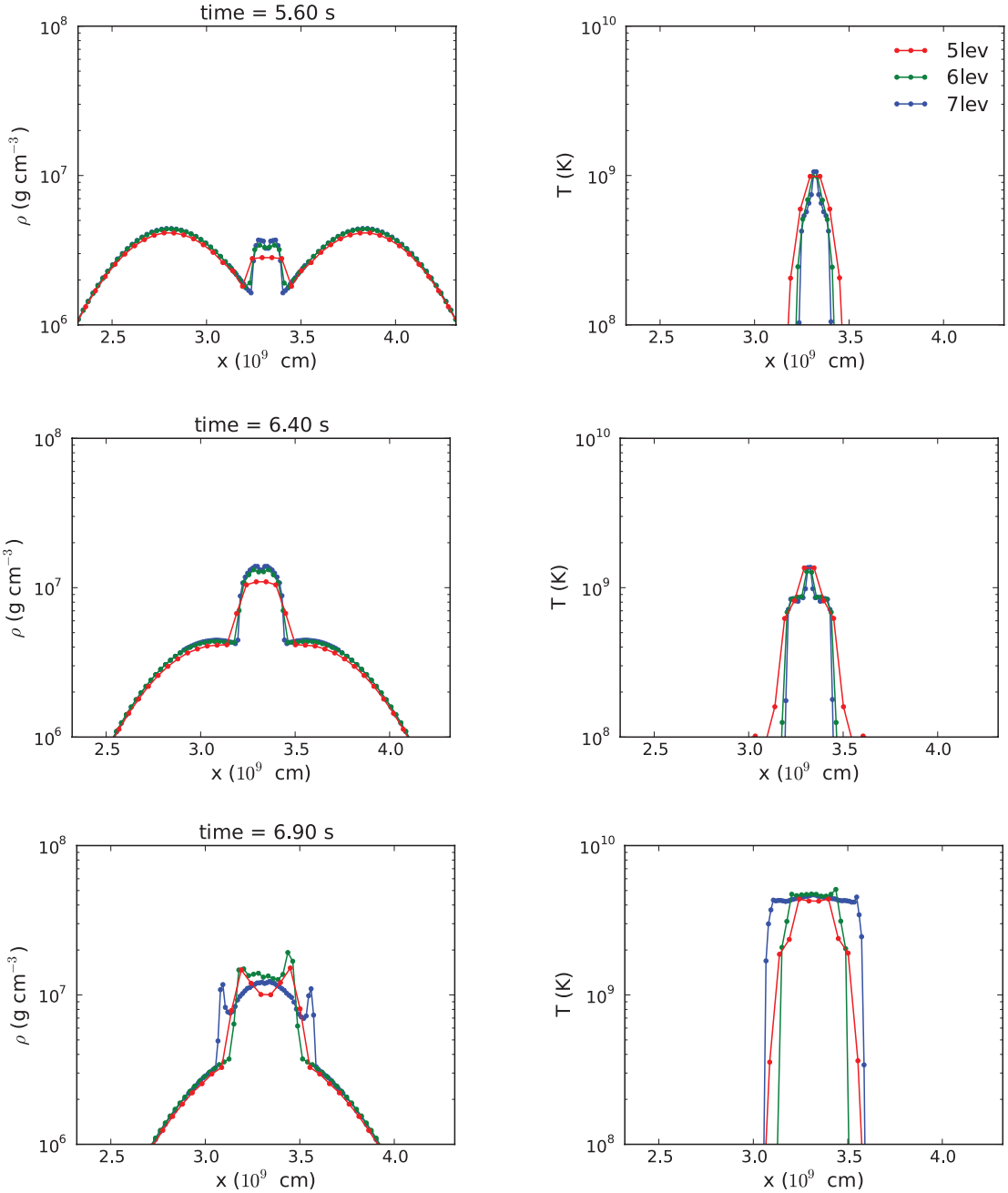

Figure 2.10: Density and temperature profiles along the x-axis for the 2×0.64 collision at 5.6 s, 6.4 s, and 6.9 s for different levels of refinement.

the 6-level or the 5-level. That is, the burning front travels farther for the same amount of time.

Unlike the 2×0.64 collision, the 2×0.81 collision produces less ^{56}Ni as level of refinement increases (see Fig. 2.8). The upper panel of Fig. 2.11 shows the three models with different spatial resolutions for the 2×0.81 collision at 4.0 s. The temperatures for all three resolutions are hot ($> 3 \times 10^9$ K), indicating the energy generated by burning is large. The shocked region is widest for the 7-level model and narrowest for the 5-level model with the 6-level model in-between. The 7-level model has the lowest, and nearly constant, density ($\approx 8 \times 10^6$ g cm^{-3}) in the stalled shock region, and has the largest magnitude spikes in the density (just below 2×10^7 g cm^{-3}) at the edges of the stalled shock. The spikes occur because the density of material is highest just behind the shock front. The 6-level model has a slightly larger ($\approx 8 \times 10^6$ g cm^{-3}), nearly constant, density in the middle, and slightly smaller spikes in the density (just below 2×10^7 g cm^{-3}) at its edges. The 5-level model has its density spikes (just above 10^7 g cm^{-3}) close enough together that a nearly constant density in the middle in barely reached.

The second panel of Fig. 2.11 shows at 4.4 s the width of the shocked, burning region is larger for all three resolutions, because the energy generated by burning in the hot shocked region is sufficient to overcome the standing shock formed from material moving inwards. That is, the shocked burning region is growing. The temperature is nearly the same and constant ($\approx 5 \times 10^9$ K) across all three resolutions, but with small spikes at the edges of each shocked region. The nearly constant density in the central region of the 7-level model is still smaller and wider than the the 6-level model. The 5-level still has its two spikes near the center, thus a nearly constant central density region is not reached.

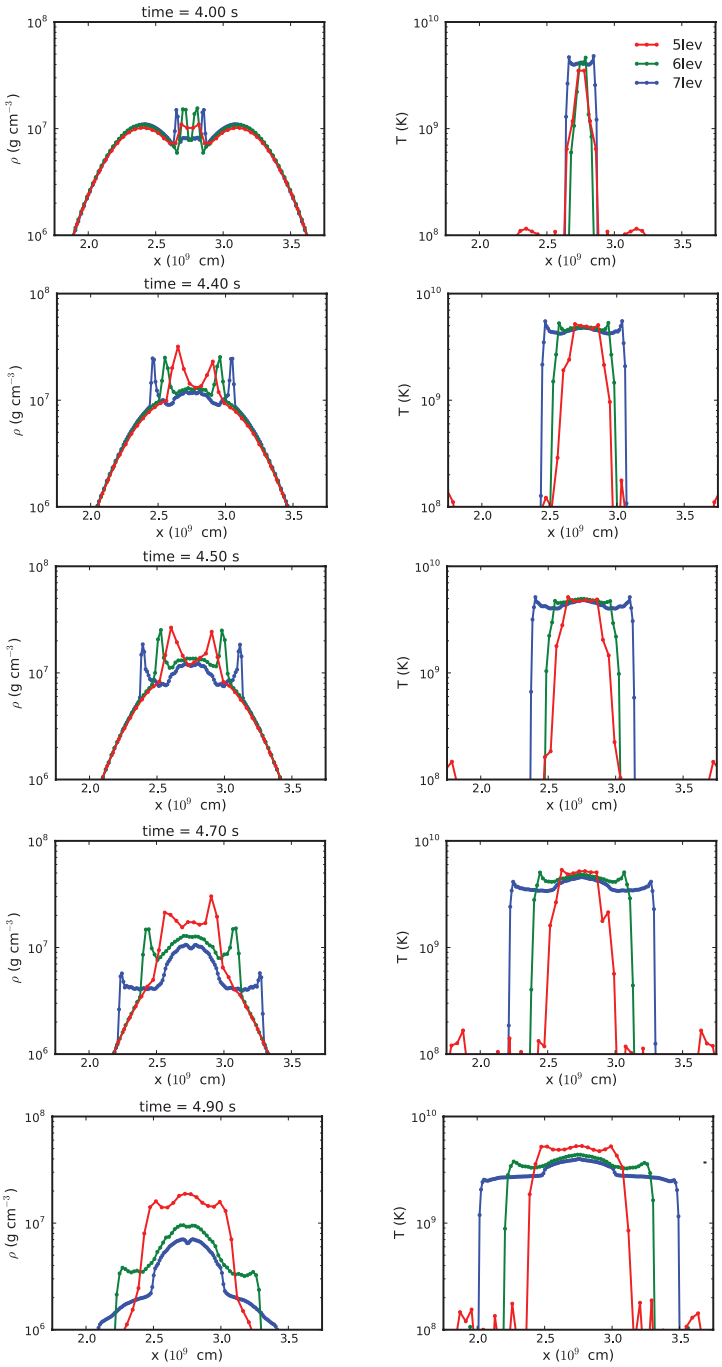

Figure 2.11: Density and temperature profiles along the x-axis for the 2×0.81 collision at 4.0 s, 4.4 s, 4.5 s, 4.7 s, and 4.9 s for different levels of refinement.

The third panel of Fig. 2.11 shows at 4.5 s the the 7 level model begins to detonate, but the 6-level and 5-level models have not yet detonated. The same patterns in density and temperature described for previous time points still hold. By 4.7 s, the fourth panel Fig. 2.11 shows the 6-level model begin to detonate, but the 5 level model has not yet detonated. The width of the burning region for the 6-level model is about the same width as the 7-level model when the 7-level model detonated 0.2 s earlier.

At 4.9 s (bottom panel Fig. 2.11), the 5-level model is the last to detonate. The 5-level model has finally reached a state of nearly constant density in the central region with spikes at the edges. This nearly constant density of 2×10^7 g cm^{-3} is larger than the nearly constant density reached by either the 6-level or the 7-level models (both about 10^7 g cm^{-3}), but it has reached about the same width. Since the 7-level model detonates at the lowest density (but the same mass since all reach about the same width before detonating) and soonest in time, the 7-level model should produce the least amount of ^{56}Ni. The 5-level model detonates at a higher density (and same mass) and latest in time, thus should produce the most ^{56}Ni. This explains the pattern in the the abundance yields with spatial resolution in Fig. 2.8.

Similarities and Differences Between the Explosion Models

Whether the explosion is initiated along the edge of the stalled shock region (as in the 2×0.81 collisions) or in the central regions of the stalled shock (as in the 2×0.64 collisions) is controlled by the initial masses of the white dwarfs, as the masses set the infall speed (escape velocity). The infall speed determines the strength of the initial shock, and thus the initial post-shock temperature. In turn, the initial post-shock temperature determines the amount of initial burning behind the shock, and hence the temperature profile of the shocked region. Comparing the temperatures profiles in the shocked region between the 2×0.64 and 2×0.81 collisions, we see that the 2×0.64 temperature barely reaches 10^9 K, while for the 2×0.81 temperature is a hot $\approx 5 \times 10^9$ K over an

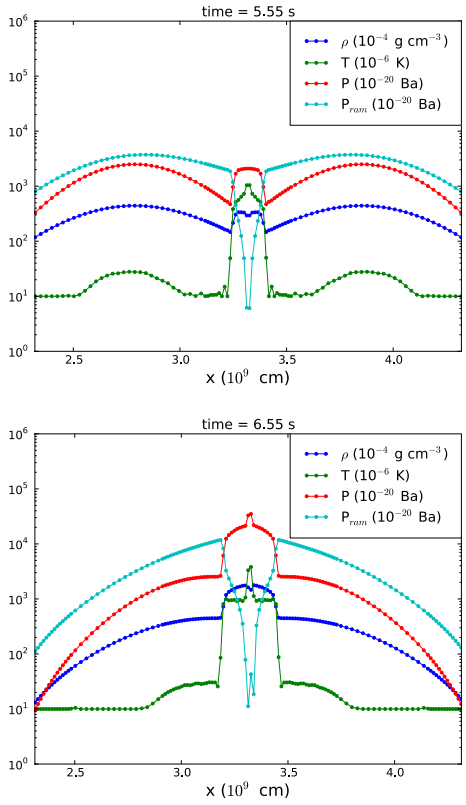

Figure 2.12: Profiles of the density, temperature, pressure, and ram pressure along the x-axis for the 2×0.64 collision at 5.55 s and 6.55 s.

extended region. The difference in the temperature between the two model collisions is a direct consequence of the kinetic energy of the collision (larger kinetic energy corresponding to larger temperature).

The initial shock in the 2×0.64 collision models barely raises the temperature above the ^{12}C+^{12}C threshold. As carbon burning proceeds, the central shocked burning region increases in temperature. The top panel of Fig. 2.12) shows the system cannot explode yet because the temperature is not hot enough to overcome the ram pressure from the infalling material, which continues to increase due to density profile of the white dwarf. When the peak of the white dwarf density profiles enters the shocked

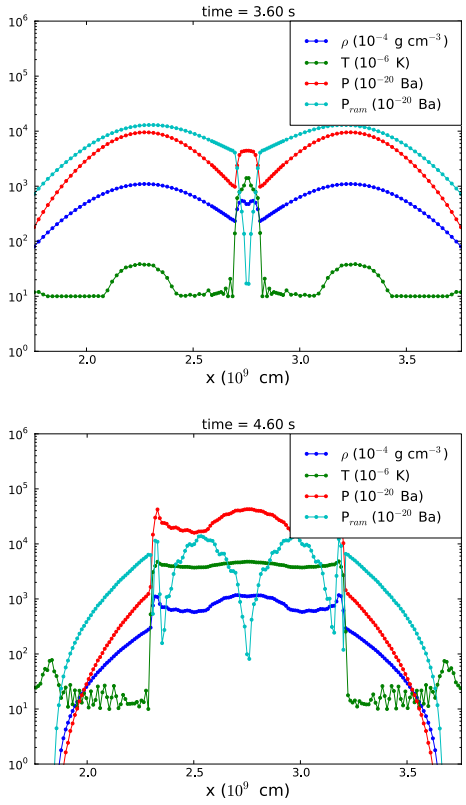

Figure 2.13: Density, temperature, pressure, and ram pressure profiles along the x-axis for the 2×0.81 collision at 3.60 s and 4.60 s.

region does the central peak undergo thermonuclear runaway, which creates enough pressure to overcome the now decreasing ram pressure (see bottom panel of Fig. 2.12).

In contrast to the 2×0.64 collision model, the 2×0.81 collision model is energetic enough that the initial shock raises the temperature well above the ^{12}C+^{12}C threshold. The entire stalled shocked region burns rapidly to a state of nuclear statistical equilibrium and achieves a nearly isothermal state. Central ignition cannot occur because the ^{12}C+^{16}O material has already lost nearly all of its energy in the burn to nuclear statistical equilibrium. The top panel of Fig. 2.12 shows, similar to the 2×0.64 collision models, the 2×0.81 collision model cannot yet explode since the ram pressure from the infalling material is greater than the pressure of the hot burned material push-

ing outwards. When the pressure inside the hot burned region is larger than the ram pressure does the system explode, giving the appearance of an edge-lit ignition (see bottom panel of Fig. 2.12).

2.4 Discussion

We have performed the first systematic study of zero impact parameter collisions between two white dwarfs with an Eulerian grid code (FLASH). Our simulations spanned a range of effective spatial resolutions for collisions between two 0.64 $M_\odot$ white dwarfs and two 0.81 $M_\odot$ white dwarfs. However, even the highest resolution studies did not achieve strict numerical convergence.

The lack of convergence in the simplest configuration (zero impact parameter, equal masses) suggest that quantitative predictions of the ejected elemental abundances that are generated by binary white dwarf collision and merger simulations should be viewed with caution. However, the convergence trends do allow some patterns to be discerned.

We found the 2×0.64 collision model head-on collision model produces 0.32 $M_\odot$ of ^{56}Ni, 0.38 $M_\odot$ of ^{28}Si, and 0.2 $M_\odot$ of unburned ^{12}C+^{16}O. Rosswog et al. (2009) included one FLASH based model of a zero impact parameter collision of two 0.60 $M_\odot$ white dwarfs in their study. They reported a ^{56}Ni mass of 0.16 $M_\odot$, about one-half of what we find. While Rosswog et al. (2009) used slightly less massive white dwarfs than our study, both sets of FLASH simulations used the same equation of state. The FLASH model of Rosswog et al. (2009) achieved about a factor of 2.6 smaller spatial resolution than our study $R = 4.9 \times 10^6$ cm versus $R = 1.3 \times 10^7$ cm), due to their evolving one white dwarf and deploying a mirrored gravitational potential. This difference in the maximum spatial resolution could account for the different ^{56}Ni masses between the two calculations, although the convergence trend shown in the upper panel Fig. 2.8

suggests spatial resolution might not be the only reason for the difference. Another potential reason for the difference in the ^{56}Ni masses is the choice of the timestep, and thus the coupling between the operator split processes of hydrodynamics and the nuclear burning. In all our simulations, we limited the timestep to $\approx$0.01 of the Courant limited hydrodynamic timestep during the nuclear burning phases (see Fig. 2.9). We found changing the allowed timestep can change the ^{56}Ni mass produced by 30% - 40%.

We find our FLASH-based, zero impact parameter, collision models systematically produce less ^{56}Ni and more silicon-group elements than collisions models calculated with SNSPH by Raskin et al. (2010). This difference between particle and grid based codes was first found by Rosswog et al. (2009), who suggested that differences in nuclear reaction networks or advection effects could be responsible for the different yields. While our FLASH models used the same equation of state and nuclear reaction network as Raskin et al. (2010), and we checked the same output values were returned for the same input values, a detailed investigation of the differences between our FLASH model results and the Raskin et al. (2010) results with SNSPH are beyond the scope of this paper.

Red and dim SNIa such as SN 1991bg (Leibundgut et al. 1993; Turatto et al. 1996; Hachinger et al. 2009) SN 1992K (Hamuy et al. 1994), SN 1999by (Garnavich et al. 2004), and SN 2005bl (Taubenberger et al. 2008) are characterized by $M_V \approx$-17. The light curves of underluminous SNIa decline even more rapidly than expected from a linear luminosity to decline-rate relation among normal SNIa (Phillips et al. 1999; Taubenberger et al. 2008; Blondin et al. 2012). Spectroscopically, 91bg-like SNIa show low line velocities around B-magnitude maximum (Filippenko et al. 1992) and clear spectral signatures of Ti-II, indicating lower ionization (Mazzali et al. 1997). Taken together, these properties together are consistent with $\sim$0.1 $M_\odot$ of newly synthesized

^{56}Ni. Our FLASH models suggest 2×0.64 $M_\odot$ and 2×0.81 $M_\odot$ head-on collision models produce ^{56}Ni masses below that needed for normal SNIa, but are within a range consistent with observations of underlumnous SNIa. In addition, either mass pairing produces ~ 0.2 $M_\odot$ of unburned C+O, which may be a unique signature of mergers and collisions between white dwarfs.

Future studies should include a survey of non-zero impact parameter white dwarf collisions with FLASH, an exploration of unequal mass collisions, and an investigation why Lagrangian particles codes and Eulerian grid codes continue to find about a factor of two difference in the mass of ^{56}Ni ejected. The zero impact parameter is insightful as an upper limit on ^{56}Ni production, but a non-zero impact parameter study will likely give a range of ^{56}Ni yields for different collision configurations. An exploration of unequal mass collisions could provide a broader physical parameter space and allow an improved quantitative description of how SNIa luminosity scales with mass pairings.

Chapter 3

NON-ZERO IMPACT PARAMETER WHITE DWARF COLLISIONS IN FLASH

Abstract

We systematically explore 3D non-zero impact parameter collisions of white dwarfs with the Eulerian adaptive grid code FLASH for 0.64+0.64 $M_\odot$ and 0.81+0.81 $M_\odot$ mass pairings. For both mass pairings, we use two impact parameters, $b = 1$ (one white dwarf radius from center to center at the time of collision), and $b = 2$ (two white dwarf radii from center to center at the time of collision). Our models span a range of effective linear spatial resolutions from 6.25×10^7 to 1.37×10^7 cm. The 5-level 0.64+0.64 $M_\odot$ collision is not energetic enough to fall on the convergence curve, however general trends in element production can be seen. We find that the 0.64+0.64 $M_\odot$ $b = 1$ collision model produces 0.0562 $M_\odot$ of ^{56}Ni and 0.494 $M_\odot$ of ^{28}Si, while the 0.81+0.81 $M_\odot$ $b = 1$ collision model produces 0.100 $M_\odot$ of ^{56}Ni and 0.656 $M_\odot$ of ^{28}Si at the highest spatial resolutions. Both mass pairings produce $\sim$0.3 $M_\odot$ of unburned ^{12}C+^{16}O. The stars lose orbital angular momentum due to a 50% increase in spin angular momentum as they approach each other. However, total angular momentum is conserved to within 25%. For the $b = 2$ case, neither mass pairing produces a significant amount of ^{56}Ni because a critical density and temperature are never achieved in the burning region.

3.1 Introduction

Supernovae Type Ia (SNIa) are among the most energetic explosions known, reaching a peak absolute magnitude of M_V $\sim$-19.2, synthesizing $\sim$0.7 $M_\odot$ of radioactive ^{56}Ni, and imparting $\sim10^{51}$ ergs of kinetic energy to their ejecta. Removing the intrinsic, systematic variation of SNIa light curves to create standard candles generally uses two quantities: the measured color, typically rest-frame BâĂŽÃăÃ■V and often

one additional optical color, and an empirically defined light curve shape parameter, such as Δm_{15} (Phillips 1993; Hamuy et al. 1996), Δ (Riess et al. 1996; Jha et al. 2007), and stretch s (Perlmutter et al. 1997; Guy et al. 2005; Conley et al. 2008), or x_i (Guy et al. 2007). The subsequent discovery of the accelerated expansion of the universe using SNIa (Riess et al. 1998; Perlmutter et al. 1999) allows SNIa to serve as probes of the dark energy equation of state, commonly parameterized by $w(z) = P/\rho$. The main challenge to measuring w(z) using SNIa is reducing the systematic errors in the measured distance modulus from the current level of about 12% to about 1% (Kim et al. 2004). One avenue for increasing the accuracy of the measured distances is attempting to homogenize the population of SNIa used for cosmological studies.

In the standard paradigm single-degenerate scenario, a carbon-oxygen white dwarf in a close binary system accretes material from its companion and grows to the Chandrasekhar mass (Iben & Tutukov 1984). As the white dwarf nears the mass limit, slow carbon burning at central densities of $\approx 2-6\times10^9$ g cm^{-3} causes the core to convectively simmer for $300-1000$ yr (Woosley et al. 2004; Piro & Chang 2008). Subsonic burning fronts are then launched from matchhead masses that attain temperatures of $\approx 8\times10^9$ K, which subsequently proceed to incinerate the white dwarf (Nomoto et al. 1984; Thielemann et al. 1986; Woosley & Weaver 1986; Khokhlov 1991; Timmes & Woosley 1992; Jordan et al. 2008; Kasen et al. 2009; Townsley et al. 2009; Woosley et al. 2011). In contrast, the double-degenerate scenario involves the dynamical coalescence of two carbon-oxygen white dwarfs to produce the desired explosion (Iben & Tutukov 1984; Webbink 1984; Benz et al. 1989, 1990; Mochkovitch & Livio 1989; Rasio & Shapiro 1994; Segretain et al. 1997; Guerrero et al. 2004). While for many years the single-degenerate scenario was the more prominent, a number of observations (Mannucci et al. 2005; Scannapieco & Bildsten 2005; Howell et al. 2006; Quimby et al. 2007; Hicken et al. 2007; Napiwotzki et al. 2007; Raskin et al. 2008; Ruiter et al. 2009; Hachinger et al. 2009; Maoz 2010; Scalzo et al. 2010; Mullally et al.

2009; Yamanaka et al. 2009; Tanaka et al. 2010; Maoz et al. 2011) have led to recent efforts to better quantify the double-degenerate scenario (Yoon et al. 2007; Maoz 2008; Raskin et al. 2009; Rosswog et al. 2009; Lorén-Aguilar et al. 2009, 2010; Pakmor et al. 2010; Raskin et al. 2010; Dan et al. 2011, 2012; Shen et al. 2012). Reviews of the various proposals for SNIa progenitors may be found in Branch et al. (1995); Hillebrandt & Niemeyer (2000); Leibundgut (2001); Nomoto et al. (2003); Howell (2011); Wang & Han (2012).

It is unknown if both single-degenerate and double-degenerate scenarios operate in reality, and if so, at what relative frequency. Pfahl et al. (2009) estimate an all-sky rate of $\approx 0.1\eta(D/100\ \mathrm{Mpc})^3\ \mathrm{yr}^{-1}$ for SNIa in globular clusters where D is the distance in Mpc, and η is the rate enhancement per unit mass. η is estimated to be about 2-10. A globular cluster SNIa could provide evidence for double-degenerate mergers. The homogeneity of the SNIa progenitor population is relevant for measuring the dark energy equation of state because younger stellar populations produce more luminous SNIa and the star formation rate increases strongly with redshift, such that the mean properties of SNIa are redshift dependent (Sullivan et al. 2006; Mannucci et al. 2006; Gallagher et al. 2008; Howell et al. 2009; Neill et al. 2009). While these dependencies can be calibrated if all supernovae obey the same stretch-luminosity relationship, and obviously peculiar SNIa are excluded, a mixture of single-degenerate and double-degenerate progenitors could be lurking in supernova surveys and possibly increasing the intrinsic scatter in the SNIa Hubble diagram.

In the previous chapter, we explored zero impact parameter collisions of white dwarfs in 3D with the Eulerian adaptive grid code FLASH for 0.64+0.64 $M_\odot$ and 0.81+0.81 $M_\odot$ mass pairings. These idealized cases – head-on collisions between identical, initially spherical white dwarfs – highlighted the essential physics and numerical convergence properties of the simplest possible configuration. In this paper, we

examine idealized collisions with non-zero impact parameters, $b = 1$ (one white dwarf radius from center to center at the time of impact) and $b = 2$ (two white dwarf radii from center to center at the time of impact; a grazing collision) in 3D with FLASH for the same mass pairings. Two aims of our paper is to determine whether or not, given our available computing resources and the numerical algorithms implemented in FLASH, simulations of non-zero impact parameter collisions can adequately conserve angular momentum and dependably predict the amount of white dwarf material that is converted into heavier elements by nuclear burning. Finally, our non-zero impact parameter idealized configurations form a baseline for further merger studies that incorporate more realistic initial conditions.

In §3.2 we discuss the input physics, initial conditions, and boundary conditions of our simulations. §3.3 addresses angular momentum conservation properties of our non-zero impact parameter double-degenerate collision models, and §3.4 presents the general properties and nucleosynthesis of the $b = 1$ and $b = 2$ collision simulations. A $b = 1$ collision means that the stars are one white dwarf radius apart at first contact while a $b = 2$ collision means that the stars are two white dwarf radii apart at first contact. Convergence trends and analysis are given in §3.5. A discussion of future work is given in §3.6

3.2 Input Physics, Initial Conditions, and Boundary Conditions

We use FLASH version 3.3 (Fryxell et al. 2000; Calder et al. 2002) with its native Helmholtz equation of state (Timmes & Swesty 2000), 13 isotope alpha-chain reaction network to model energy generation from nuclear burning from ^{4}He to ^{56}Ni (Timmes 1999), and the multigrid Poisson gravity (Ricker 2008). We use the diode boundary condition, which is a zero-gradient boundary condition where fluid velocities are not allowed to point back into the domain.

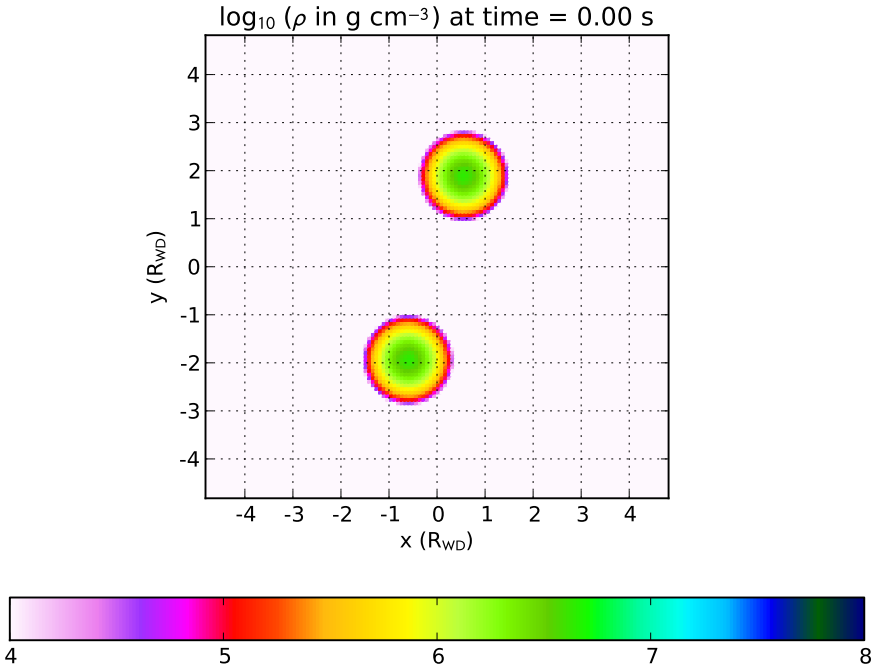

Figure 3.1: A 2D slice of density through the x-y mid-plane at t=0.0 seconds for the $b = 1$ 0.64+0.64 $M_\odot$ collision. Each tick mark has a value of one white dwarf radius, which is 8.3×10^8 cm. The white dwarfs are positioned four white dwarf radii apart from center to center. The x-direction offset to produce a $b = 1$ impact is determined by a two-body solver from Raskin et al. (2010).

We calculate the 1D white dwarf profiles for two masses, 0.64 and 0.81 $M_\odot$, under the assumptions of hydrostatic equilibrium and mass conservation. We use the Helmholtz equation of state, as does FLASH, and assume a composition of equal parts ^{12}C and ^{16}O with an isothermal temperature of 10^7 K. The 1D structure of the white dwarf models were verified with MESA (Paxton et al. 2011). The 1D white dwarf profiles are mapped onto a 3D rectilinear Cartesian grid with a box size set to the smallest computational domain size that does not allow a significant amount of mass leaving the grid before runaway nuclear burning takes place in the b=1 case for each

mass pair (8×10^9 cm for the 0.64+0.64 $M_\odot$ mass pair, and 7×10^9 cm for the 0.81+0.81 $M_\odot$ mass pair).

The white dwarfs are initially placed four white dwarf radii apart from center to center (see Fig. 3.1), allowing for the evolution to exchange angular momentum and produce tidal distortions while maintaining sufficient numerical resolution near the centers of the white dwarfs. The initial velocities are calculated by using a two-body solver, which implements a Runge-Kutta integration with an adaptive time step, assuming globular cluster velocity dispersion of $\sigma = 10$ km/s as described by Raskin et al. (2010). The white dwarfs are given x and y velocities such that they will make first contact with the specified impact parameter.

The surrounding ambient medium is set to the same temperature as the isothermal white dwarfs with a density that is small (10^{-4} g cm^{-3}) compared to the density of the outermost regions of the white dwarf ($\sim$1-10 g cm^{-3}). Table 3.1 lists the initial conditions for each of our ten simulations.

Table 3.1: Initial Conditions for the 3D FLASH models. Columns are run number, white dwarf masses (M_1, M_2), impact parameter (b), maximum level of refinement (l), maximum spatial resolution (R), box size (D), white dwarf initial velocities (v_x, v_y), white dwarf radius (R_{WD}), and white dwarf central density (ρ_{WD}).

#	M_1, M_2 ($M_\odot$)	b	# l	Max. R (10^7 cm)	D (10^9 cm)	$v_{x_{1,2}}$ (10^8 cm/s)	$v_{y_{1,2}}$ (10^8 cm/s)	R_{WD} 10^8 cm	ρ_{WD} 10^6 g/cm^3
1	0.64	1	5	6.25	8.0	$\pm$4.29	$\pm$1.93	8.30	4.51
2	0.64	1	6	3.13	8.0	$\pm$4.29	$\pm$1.93	8.30	4.51
3	0.64	1	7	1.56	8.0	$\pm$4.29	$\pm$1.93	8.30	4.51
4	0.64	2	5	6.25	8.0	$\pm$4.00	$\pm$1.93	8.30	4.51
5	0.64	2	6	3.13	8.0	$\pm$4.00	$\pm$1.93	8.30	4.51
6	0.81	1	5	5.47	7.0	$\pm$3.57	$\pm$1.56	6.88	11.2
7	0.81	1	6	2.73	7.0	$\pm$3.57	$\pm$1.56	6.88	11.2
8	0.81	1	7	1.37	7.0	$\pm$3.57	$\pm$1.56	6.88	11.2
9	0.81	2	5	5.47	7.0	$\pm$3.16	$\pm$1.56	6.88	11.2
10	0.81	2	6	2.73	7.0	$\pm$3.16	$\pm$1.56	6.88	11.2

3.3 Angular Momentum Conservation

Angular momentum in grid-codes is poorly-studied thus far, with only a select few publications addressing the topic. Marcello & Tohline (2012) study a numerical method for investigating super-Eddington mass transfer in double-degenerate binary systems, and they assume that most of the changes in angular momentum are due to errors in the numerical method. They show angular momentum conserved to within a relative error of 1.7×10^{-6} per orbit. Another study on mass transfer in binaries (Motl et al. 2002) gives a relative error of $\approx 10^{-4}$ per orbit.

Angular momentum is an inherently circular phenomenon, and thus it is classically considered to be poorly conserved in FLASH, a grid-based code. However, our angular momentum analysis tells a different story. Fig. 3.2 shows the angular momentum for the 0.64+0.64 case where the 5- and 6-level are run from t=0 seconds. Fractional angular momenta are shown with respect to the initial total angular momentum, in this case 1.52×10^{50} g cm^2 s^{-1}. Angular momentum is given by $J = L + S$, where L is the orbital angular momentum and S is the spin angular momentum. L is calculated by taking the angular momentum around the system center of mass. The spin angular momentum S is then the sum of the angular momenta for the material in each star with respect to that star's center of mass.

Spin angular momentum is only shown to first contact (t=2.96 seconds) as after that the material on either side of the grid becomes mixed and there is difficulty telling what material belongs to what star. The spin angular momentum up to first contact is conserved to within 1%, indicating that the white dwarfs do not "spin up." Total angular momentum stays conserved to within 15% before first contact, then drops as the stars begin their nuclear burning phase, dropping to the lowest point between 5 and 6 seconds, then returning to within 10% of the original angular momentum value near

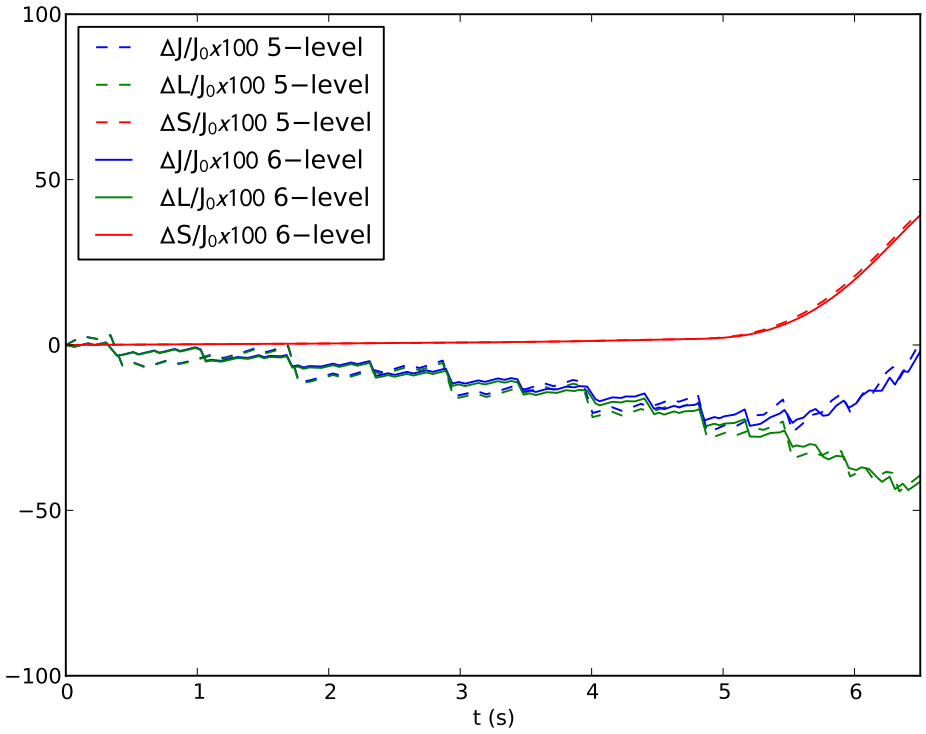

Figure 3.2: Angular momentum for the 0.64+0.64 case, where the total angular momentum is $J = L + S$, where L and S are orbital and spin angular momentum respectively. For this series of runs, the 5- and 6-level were both started from t=0 s. All fractional changes are with respect to the initial total angular momentum.

uniform expansion. The total angular momentum is fairly well-conserved to within about 25%. The 5- and 6- level runs agree in angular momentum conservation to within 1%.

To eliminate any differences between runs for dynamics that happen before first contact, the 6- and 7-level runs were run from the 5-level first contact checkpoint file. The angular momentum for the "from first contact" runs is shown in Fig.3.3. Again, the spin angular momentum before first contact doesn't change to within 1%, then the material becomes mixed and the spin angular momentum is no longer displayed. At first contact, where the 6- and 7-level runs begin, and show better angular momentum

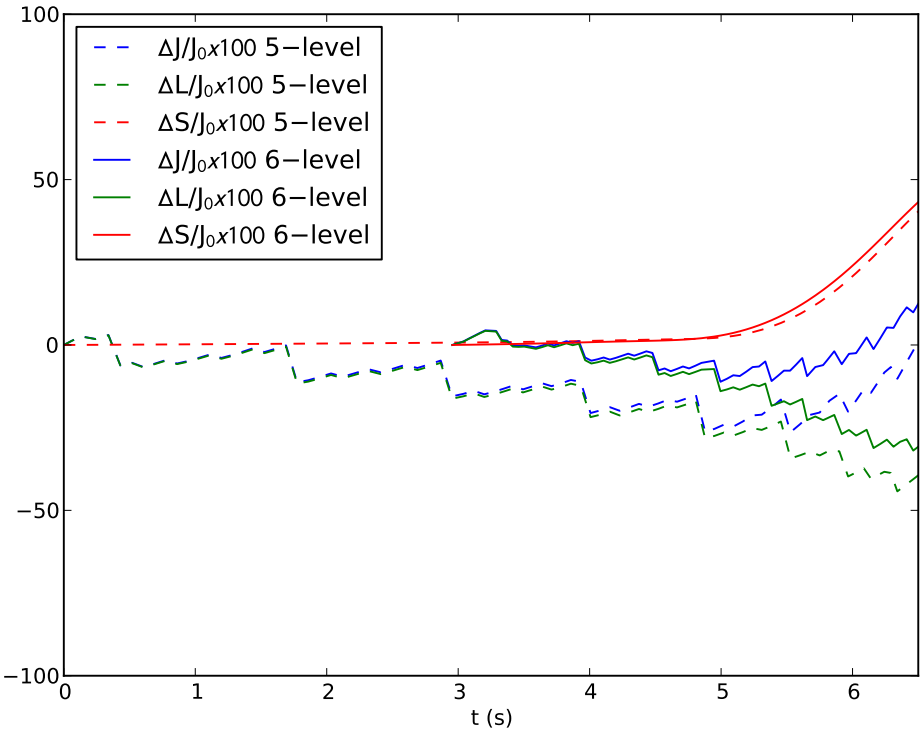

Figure 3.3: Angular momentum for the 0.64+0.64 case, where the total angular momentum is $J = L + S$, where L and S are orbital and spin angular momentum respectively. For this series of runs, the 6-level was started from the 5-level run just before first contact. All fractional changes are with respect to the initial total angular momentum.

conservation than the runs from t=0. The angular momentum curves are the same between the 6- and 7-level to within 1%, and they conserve angular momentum to within 15%. They follow the same pattern as the 5-level, dropping between 5 and 6 seconds, then returning to a higher value (within 1% of the original angular momentum value) near uniform expansion.

3.4 Runs

0.64+0.64 b=1 Collision

Fig. 3.4 shows the starting point of the 0.64+0.64 $b = 1$ collision. The simulation was run to 2.96 seconds at $l = 5$, then restarted using $l = 7$. At this time, the white

dwarfs are in a pre-first-contact configuration, and the low $l = 5$ spatial resolution is noticeable. The top-left panel of Fig. 3.4 shows the density-temperature profile for the cells (each cell is represented by a point, then the points are binned by 100 equally spaced bins in logarithmic density and temperature space). The color of each point represents the most prominent species in the cells, with green corresponding to ^{12}C, blue corresponding to ^{28}Si, and red corresponding to ^{56}Ni. At t=2.96 seconds, all the points are green, indicating that all the cells are primarily composed of ^{12}C. The cold, un-shocked material has $T < 10^8$ K and $\rho < 10^{6.5}$ g cm^{-3}. The lineout profile in the bottom left shows temperature, density, velocity and sound speed along the line of centers. The same density and temperature features mentioned above are shown in this plot, and the sound speed $c_s < 4 \times 10^8$ cm/s, less than the infall velocity. The centers are 2.2×10^9 cm apart.

At t=4.07 seconds (see Fig. 3.5), the stars are at first contact. Most of the material is still in the unshocked, cold, sparse region. There is a new region in the upper left diagram with $\rho < 10^5$ g cm^{-3} and $T < 10^9$ K indicating the shocked material. The same density features are seen in the diagram on the right. The centers are 1.8×10^9 cm apart and $c_s < 3 \times 10^8$ cm/s, less than the infall velocity.

At t=6.55 seconds (see Fig. 3.6), the stars have started producing ^{28}Si (blue points in the upper left pane). A hot, dense region ($T > 10^9$ K, $\rho > 10^{6.5}$ g cm^{-3}) in the density-temperature plane indicates the first signs of runaway nuclear burning. In the right pane, a lenticular region of high density is visible where ^{28}Si generation is occurring. The sound speed is now higher than the infall velocity in the center.

At t=6.75 seconds (see Fig. 3.7), the upper left pane indicates that more ^{28}Si as being produced, as well as ^{56}Ni. Temperature peaks along the edges of the runaway burning region at $T = 8 \times 10^9$ K, and is steady through the center at $T = 5 \times 10^9$ K. The sounds speed is steady at $c_s = 6 \times 10^8$ cm/s within the runaway burning region,

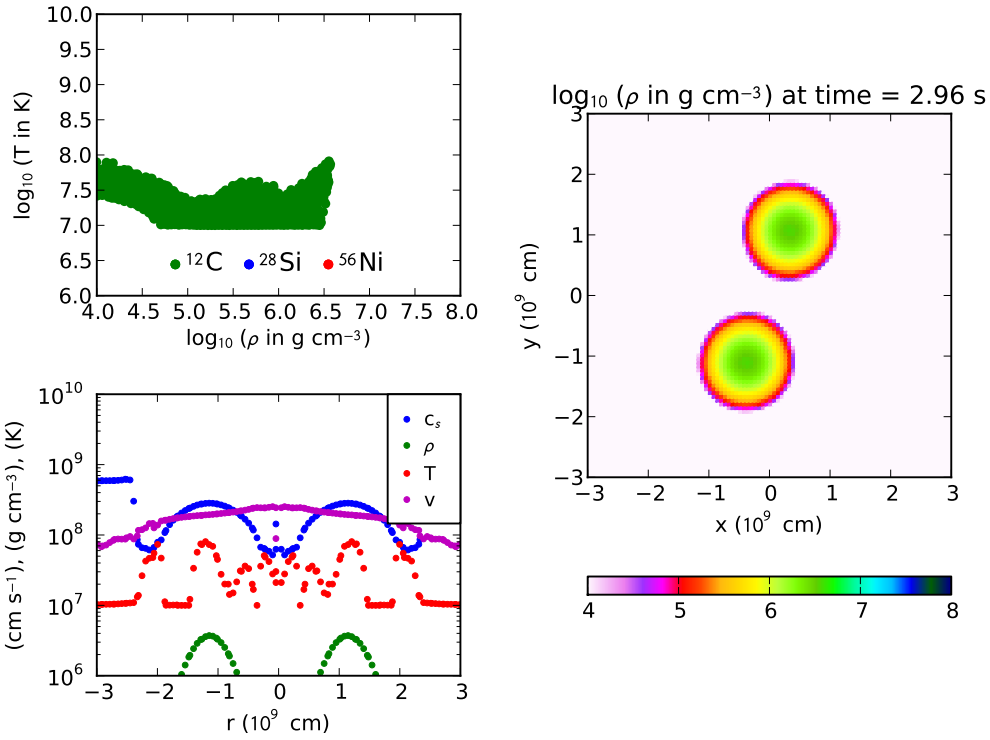

Figure 3.4: Analysis images of the 2×0.64 b=1 collision at t=2.96 s when the conversion is made from 5 to 7 levels. Top-left: Locations of all cells in the density-temperature plane. The color of the points represents the primary composition of the corresponding cell: green for ^{12}C, blue for ^{28}Si, and red for ^{56}Ni. The data are binned into 100 equally spaced bins in logarithmic density and temperature. Bottom-left: Temperature, density, and sound speed along the line of centers. Right: A 2D slice of density through the x-y mid-plane.

higher than the infall velocity, as indicated by the lower right pane. The density peaks at 2×10^7 g cm^{-3} at the edges of the runaway burning region and is steady through the center at 10^7 g cm^{-3}. The burning region is 0.4×10^9 cm wide.

At t=7.30 seconds (see Fig. 3.8), as uniform expansion is almost reached, the burning front is 1.2×10^9 cm wide with temperature and sound speed both steady through to the center at 3×10^9 K and 6×10^8 cm/s respectively. Density peaks at

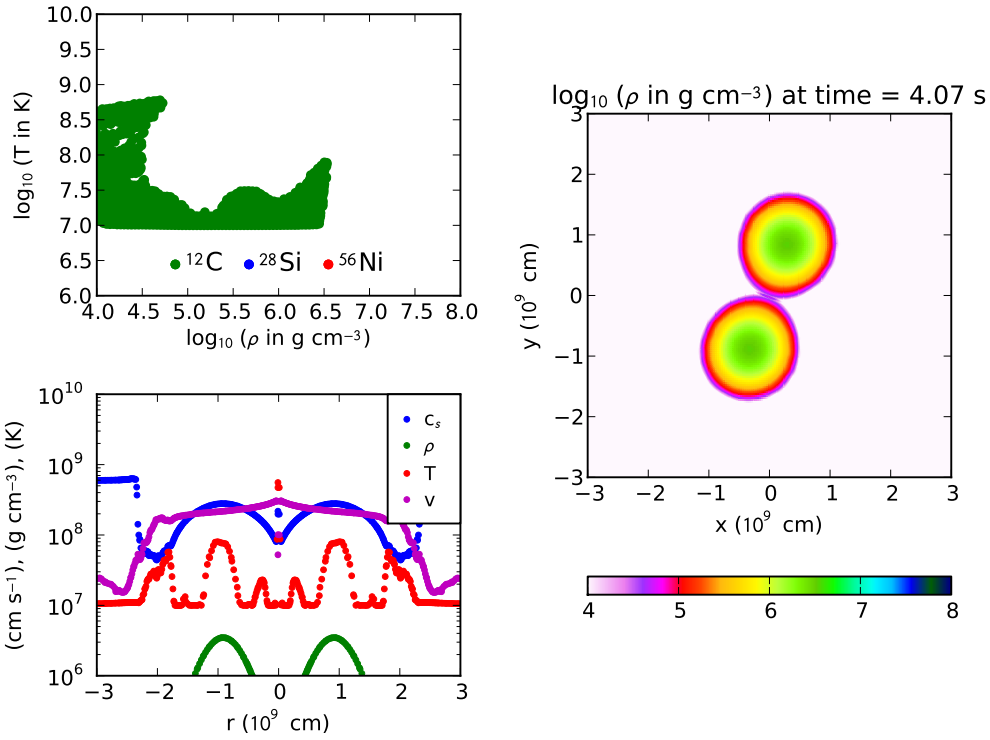

Figure 3.5: Same format as Fig. 3.4, when the model is at t=4.07 s, at first contact.

the edge of the burning region and at the center, but is nearly constant at 5×10^6 g cm^{-3}.

0.81+0.81 b=2 Collision

For both $b = 2$ collisions, runaway nuclear burning does not occur and no significant amount of ^{56}Ni is produced. A 3D figure displaying the two white dwarfs just after first contact is shown in Fig. 3.9. The white dwarfs spiral around each other several more times, but do not merge into a single object within the first 100 seconds after the collision. As the $b = 2$ runs produces little to no ^{56}Ni, we establish the SNIa production above $b = 1$ at masses less than or equal to 0.81 M$_\odot$ are unlikely, however higher mass

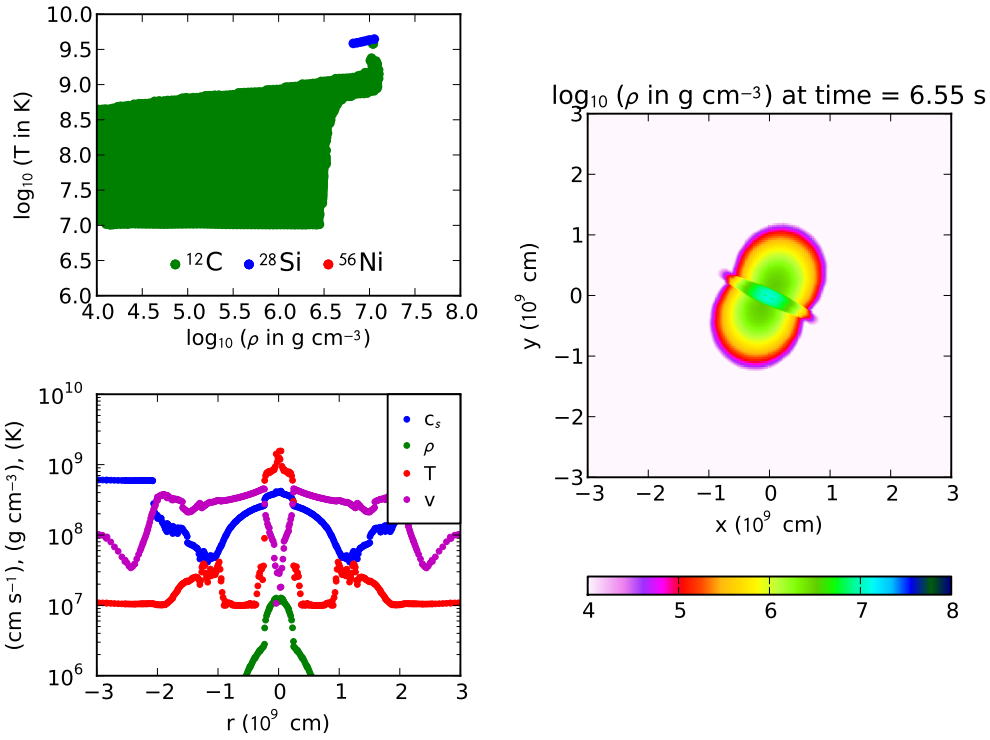

Figure 3.6: Same format as Fig. 3.4, when the model is at t=6.55 s, just before runaway burning begins.

collisions could produce increased ^{56}Ni values. Thus, we haven't ruled out higher mass $b = 2$ collisions as SNIa progenitors.

3.5 Convergence and Lineouts

Table 3.2 shows the final isotope masses for the 0.64+0.64 and 0.81+0.81 $b = 1$ collisions. The same data are displayed in graph form in Fig. 3.10.

The 7-level is the first to reach the temperature necessary for runaway nuclear burning to commence. For $l = 7$, $\rho_{max} > 1.5 \times 10^7$ g cm^{-3} with $\rho_{center} = 1.5 \times 10^7$ g cm^{-3} and $l = 7$, $T_{max} = T_{center} = 3.5 \times 10^9$ K. At the time that the 7-level reaches this temperature, the 5- and 6-level are not yet dense or hot enough to do the same. At

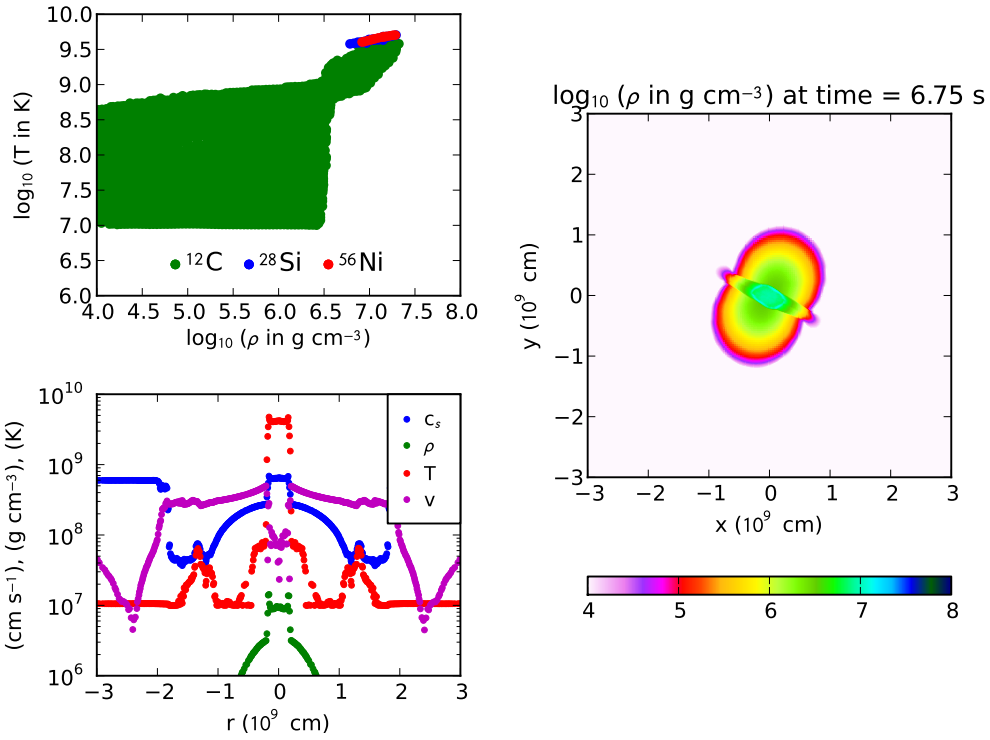

Figure 3.7: Same format as Fig. 3.4, when the model is at t=6.70 s, after runaway burning has begun.

Table 3.2: Ejected Masses.

m_1, m_2 ($M_\odot$)	b	# Levels	$^{12}C + {}^{16}O$ ($M_\odot$)	^{28}Si ($M_\odot$)	^{56}Ni ($M_\odot$)
0.64	1	5	0.424	0.486	0.0128
0.64	1	6	0.319	0.476	0.0765
0.64	1	7	0.315	0.494	0.0562
0.81	1	5	0.300	0.524	0.304
0.81	1	6	0.298	0.643	0.132
0.81	1	7	0.334	0.656	0.100

t=6.60 seconds (Fig. 3.11), for $l = 5$, $\rho_{max} = 10^7$ g cm^{-3} and $T_{max} > 1.5 \times 10^9$ K. For $l = 6$, $\rho_{max} = 1.5 \times 10^7$ g cm^{-3} an $T_{max} = 1.5 \times 10^9$ K.

The 6-level is the second to reach the conditions for runaway nuclear burning. More material has accumulated in the central dense, hot region, so the ^{56}Ni yield

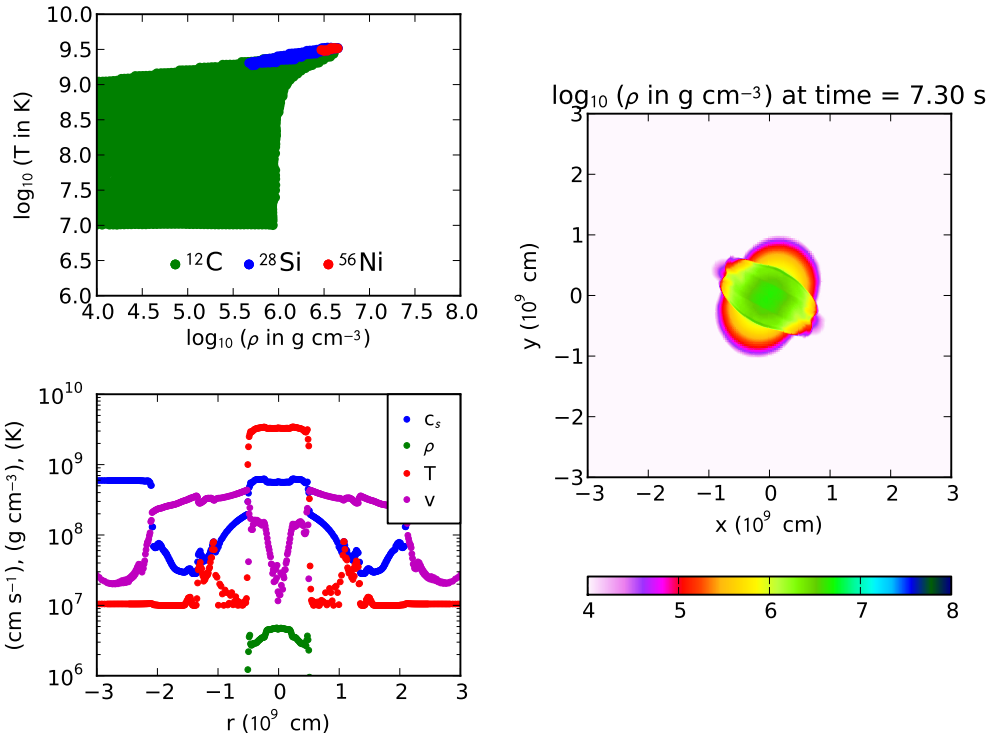

Figure 3.8: Same format as Fig. 3.4, when the model is at t=7.30 s, during the expansion phase.

is higher. For $l = 6$, $\rho_{max} = 1.5 \times 10^7$ g cm^{-3} and $T_{max} = 2.5 \times 10^9$ K. The 5-level still hasn't reached the conditions necessary for runaway nuclear burning. At t=6.80 seconds (Fig. 3.11), for $l = 5$, $\rho_{max} > 10^7$ g cm^{-3} and $T_{max} > 4.0 \times 10^9$ K. And for $l = 7$, runaway burning is already underway, so ρ_{max}=$\rho_{center} = 1.5 \times 10^7$ g cm^{-3} and $T_{max} = 5 \times 10^9$ K with $T_{center} = 4.0 \times 10^9$ K.

When the 5-level does meet the necessary criteria, runaway burning commences, but at a lower density than it happened in the 6- and 7-level cases. Finally, at t=6.90 seconds (Fig. 3.11), for $l = 5$, $\rho_{max} = 1.5 \times 10^7$ g cm^{-3} and $T_{max} > 4.0 \times 10^9$ K. For $l = 6$, $\rho_{max} > 2.0 \times 10^7$ g cm^{-3} and $T_{max} > 5.0 \times 10^9$ K with $T_{center} = 4.0 \times 10^9$ K. And for $l = 7$, ρ_{max}=$\rho_{center} = 10^7$ g cm^{-3} and $T_{max} = 5 \times 10^9$ K with $T_{center} = 4.0 \times 10^9$ K.

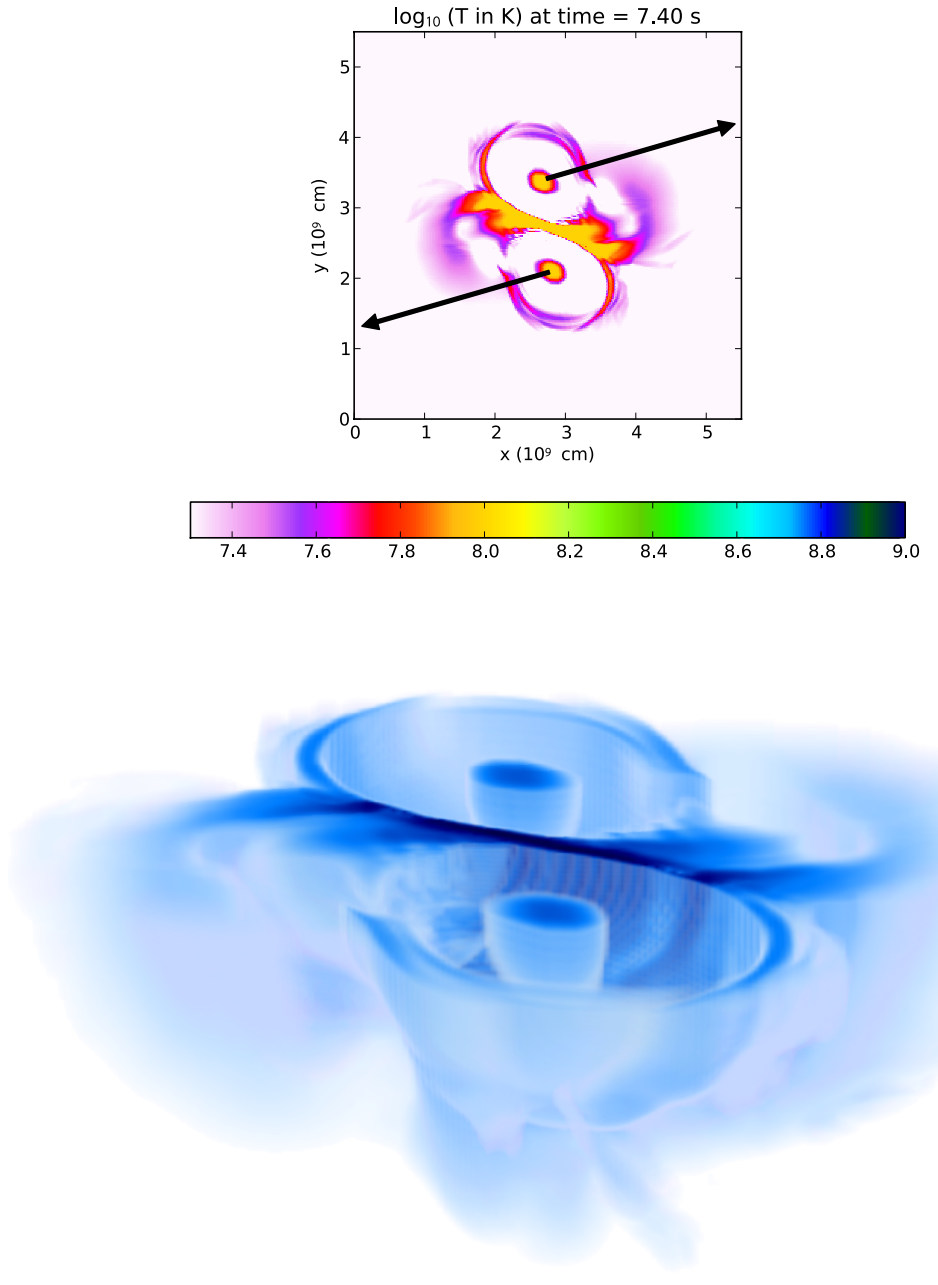

Figure 3.9: A slice through the line of centers of temperature in the z direction of a 3D figure for the 0.81+0.81 b=2 collision at t=7.4 seconds. The arrows are representative of the velocity vectors at each star's center of mass.

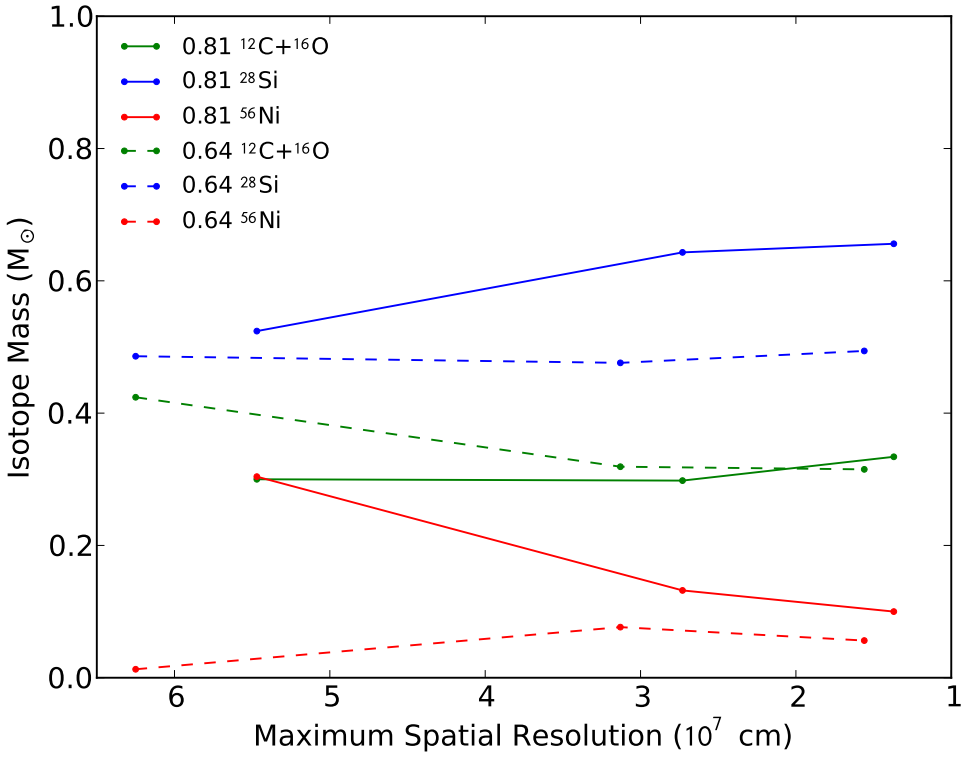

Figure 3.10: Convergence plot for the 0.64+0.64 and 0.81+0.81 cases. Although convergence is not definitively reached, some trench can be seen in isotope production.

Given the trends seen in the lineout plots, it becomes apparent that the later runaway burning starts, the more ^{56}Ni is produced, except in the case where the density in the central region is too low to produce sufficient ^{56}Ni. We believe that in this case, the 5=level run is doesn't have the necessary resolution to put it on the convergence trend. If it did, it would have produced more ^{56}Ni than the 6- and 7-level runs. However, because of the higher energy in the 0.81+0.81 case, the convergence trend is what we expect. Namely, the higher the resolution, the earlier the runaway burning starts, and the less ^{56}Ni is produced. This is the expected result.

Raskin et al. (2010) performed a similar study using SNSPH simulations for non-zero impact parameter white dwarf collisions. They found that for $b = 1$, the

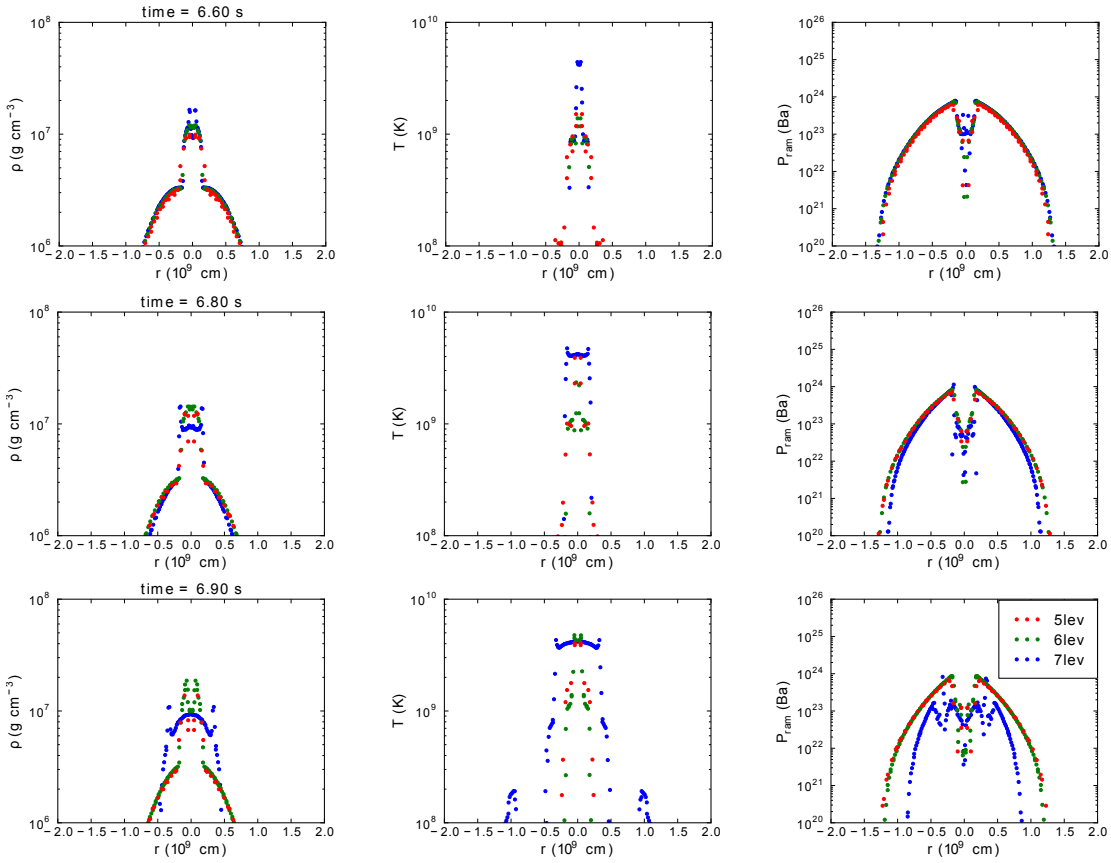

Figure 3.11: A comparison of the lineouts for the 0.64+0.64 $M_{\odot}$

collisions produced nearly the same, if not more, ^{56}Ni than the $b = 0$ case, and that most of the $b = 2$ collisions resulted in remnants. Our results differ in that they indicate less ^{56}Ni produced in the $b = 1$ case, but agree in that the $b = 2$ cases produce remnants.

3.6 Future Work

Higher resolution studies are needed to reach definite convergence. Although higher resolution studies are currently prohibitively expensive, they would nonetheless be scientifically insightful. While convergence has not been reached in this study, general trends can still be seen. These trends disagree with the results of concurrent SPH studies. Thus, a further analysis of differences between FLASH and SPH are necessary.

Additionally, the simplified initial conditions presented in this study could be expanded upon to include mergers from a binary orbit.

Chapter 4

DISCUSSION AND FUTURE WORK

In Chapter 1, I set out to answer four questions pertaining to this work: 1) Do collisions produce enough ^{56}Ni to make them supernova progenitor candidates? 2) Are there other observational signatures besides ^{56}Ni to which we can direct our attention? 3) What parameters determine yields from mergers? 4) Are current results robust with respect to spatial resolution in literature?

Let's address them each one-by-one. To answer question 1, yes, some of the collisions in this work produce enough ^{56}Ni to make them candidates for subluminous type Ia supernova progenitors. The collisions that produce the most ^{56}Ni are of higher mass (0.81 solar masses) and in a head-on configuration. Lower masses and off-center collisions produce less ^{56}Ni, and b=2 (grazing) collisions produce virtually none. In the next section, I will address why expanded parameter space (including more impact parameters and other masses) is important in this work.

To answer question 2, while we primarily look at ^{56}Ni, we also find notable ^{28}Si abundances, as well as other intermediate mass elements. Further work on this topic would include a study of the velocity structure of the abundances. Previous work by groups such as Altavilla et al. (2009) suggest that the ratio R(Si II) of intermediate-z and high redshift supernova as well as subclassification can help reduce systematic uncertainties due to dust extinction. Foley & Kasen (2011) find that there is a correlation between the intrinsic color of SNIa and their ejecta velocity. Taking into account the different in intrinsic color helps reduce the scatter in the Hubble residuals. Additionally, we would investigation into post-processing the data with a more extensive nuclear reaction network and synthesizing light curves and spectra for these collision scenarios.

Concerning question 3, we have only carried out collisions at $b = 0$, $b = 1$, and $b = 1$. We have yet to do a merger simulation involving binaries with Roche lobe overflow. Pakmor et al. (2010) performed a merger simulation for white dwarf with high masses (0.9 and 1.1 solar masses), and found that the ^{56}Ni mass was in the range of a typical SNIa and that the synthetic spectra agree well with observations. However, this study was conducted at white dwarf masses well above the statistical norm (about 0.6 solar masses) and assumes that a detonation occurs during the process of merging. Raskin et al. (2012) find that SPH calculations of white dwarf mergers at different masses most often produce a cold degenerate core surrounded by a hot disk, and they find that some of the higher mass mergers produce helium detonations at the surface. However, incorporating additional physics is needed to understand the evolution of the mergers beyond the regime where hydrodynamics and nuclear burning dominate. For example, radiative losses from the surface need to be incorporated as the disks around the cores are optically thick. It seems, at least preliminarily, that the mass of the white dwarfs is a major driver in the outcome of a merger, with higher masses producing results that point toward the possibility of white dwarf mergers as progenitors of SNIa. To more fully understand the parameters involved in a white dwarf merger calculation, we would need to implement our FLASH routine in a merger configuration for a variety of masses and include physics such as radiative loss.

Finally, to answer question 4, although we are able to see trends in the abundances from collisions, more spatial resolution would be necessary in order to create a robust set of results. For both the head-on and non-zero impact parameter cases, general trends in ^{56}Ni production are seen. We find that the 0.64+0.64 $M_\odot$ head-on collision model produces 0.32 $M_\odot$ of ^{56}Ni and 0.38 $M_\odot$ of ^{28}Si, while the 0.81+0.81 $M_\odot$ head-on collision model produces 0.39 $M_\odot$ of ^{56}Ni and 0.55 $M_\odot$ of ^{28}Si at the highest spatial resolutions. Both mass pairings produce $\sim$0.2 $M_\odot$ of unburned ^{12}C+^{16}O. We find that the 0.64+0.64 $M_\odot$ $b = 1$ collision model produces 0.0562 $M_\odot$ of ^{56}Ni and 0.494 $M_\odot$

of ^{28}Si, while the 0.81+0.81 $M_\odot$ $b = 1$ collision model produces 0.100 $M_\odot$ of ^{56}Ni and 0.656 $M_\odot$ of ^{28}Si at the highest spatial resolutions. Both mass pairings produce $\sim$0.3 $M_\odot$ of unburned ^{12}C+^{16}O. The section below about Computer Resources gives more information about how future studies can improve upon those already in the literature.

4.1 Expanded Parameter Space

This work only addresses two masses at three impact parameters, 0.64 and 0.81 $M_\odot$ at $b = 0$, $b = 1$, and $b = 2$. We choose these masses because 0.64 is very near the peak of the distribution of white dwarf masses, and 0.81 is slightly larger and allows for a second data point. The impact parameters range from head-on to grazing to represent a variety of configurations plausible for a collision. We only consider one composition, half carbon and half oxygen, because that is the simplest composition to model.

Higher mass collisions could produce interesting results, especially in the $b = 2$ case where lower masses do not reach a critical density and temperature in the burning region to produce significant amounts of ^{56}Ni. However, these higher masses require an extra step not incorporated into the current model. The isothermal white dwarfs oscillate in size by a small amount when the simulation starts, producing a higher temperature center to the stars. Therefore an isothermalization routine is suggested to remedy this problem. The routine would force the stars to remain isothermal through the oscillations until they reach an equilibrium.

Unequal mass collisions would provide perspective on the symmetry of the problem and would also fill in parts of the parameter space. With an unequal mass collision, we could see how the ejected isotopes scale by secondary mass, and what the resulting shape of the coalesced object would be impacted. This is especially useful in helping guide future high-resolution observations of white dwarf binary systems, as likely they will not have perfect mass symmetry.

4.2 Computer Resources

A study with a full range of masses and impact parameters would allow trends in ^{56}Ni to become more apparent. While this work has strived to use physically simplistic models (collisions) in order to use improved physics and equation of state, further work is required to make a more physically realistic model (merger). These calculations provide a stepping stone to a merger scenario, but a large amount of computational resources is needed to carry out the merger simulations.

Our most resolved 3D models required at least 200,000 CPU hours per run. Increasing by one level of refinement would mean increasing the number of blocks by a factor of 8 (2^3) and increasing the timestep by at least a factor of two. This would increase our CPU time by an order of magnitude or more. We can offset this effect somewhat by using more aggressive derefinement criteria or restricting the domain size, but we still expect that increasing the maximum resolution another factor of two would require ≈ 2 million CPU hours per run, which is beyond our capabilities here.

Increased spatial resolution is necessary to see further convergence trends. In both the zero and non-zero impact parameter studies, complete convergence is not reached. In the non-zero impact parameter study, one of the runs produced a collision that wasn't energetic enough to make it onto the convergence curve. High resolution studies would permit a fuller understanding of the trends in convergence that we see.

4.3 Comparison with SNSPH Simulations

A comparison between grid and particle codes could explain the discrepancies in results between the two. While studies have been done separately on collisions in each type of code, a full side-by-side comparison of the two has not been conducted. In order

to understand why FLASH results differ from SPH results, such a study would be extremely enlightening.

We compare our white dwarf collision results from FLASH to the results from SNSPH for the same initial conditions (white dwarf masses, initial separations and velocities). Our comparison indicates that FLASH produces less ^{56}Ni for the same initial conditions. For the 0.64-0.64 collision, the FLASH simulation produced 0.32 $M_{\odot}$ as compared to 0.48 $M_{\odot}$ in SPH. Similarly, the 0.81-0.81 collision produces 0.45 $M_{\odot}$ in FLASH and 0.84 $M_{\odot}$ in SPH. The inequity of ^{56}Ni values is likely due to differences in ignition criteria between FLASH and SPH. Fig. 4.1 shows a comparison between the temperature, x-axis velocity, density, and sound speed for FLASH and SPH at two times. The white dwarfs make first contact at the same time, but shortly after the collision commences two different physical scenarios ensue. At 6.60 seconds (left side of Fig. 4.1) the FLASH collision has already ignited in the center, while the SPH collision has yet to detonate. When detonation occurs in SPH, it happens along the edge of the stalled shock region, allowing for the burning of more material. At 7.25 seconds (right side of Fig. 4.1) the FLASH simulation has already reached expansion, while the SPH simulation is still synthesizing ^{56}Ni, leading to higher ^{56}Ni production in the SPH simulation.

Richardson et al. (2010) developed a tool to take Lagrangian-based SPH simulations and convert them for Eulerian-based AMR schemes, in particular for FLASH. Each particle is mapped to the cell centers via their smoothing kernel. First mapped is density, later normalized to ensure mass conservation, with the final density in a given cell equal to a linear addition of each particle's contribution. Subsequently, specific momentum and total energy are mapped by a mass weighted addition of each particle's value, later renormalized by the cell's mass. Through this, energy, mass, and momentum are conserved between the two schemes. Once the SPH-to-FLASH

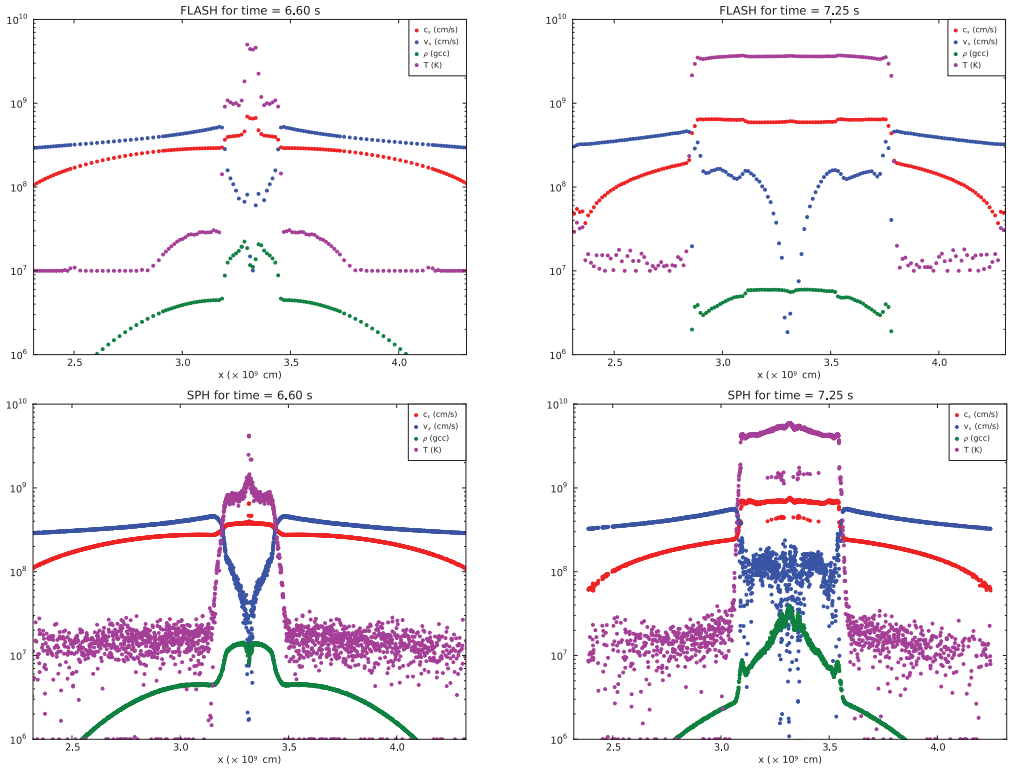

Figure 4.1: Comparison of the detonation structures in FLASH (top) and SNSPH (bottom) at t=6.60 s (left) and t=7.25 s (right) for the 0.64-0.64 case.

mapping is complete, the simulation is progressed forward in FLASH until the homologous expansion phase. Fig. 4.2 shows the density mapping from SPH to FLASH at first contact (determined visually from a logarithmic density plot) between the white dwarfs for the 0.64-0.64 $M_\odot$ case. For the 0.64-0.64 $M_\odot$ and 0.81-0.81 $M_\odot$ collisions the SPH-to-FLASH mapping produced results similar to the comparable FLASH runs. The ^{56}Ni produced in the FLASH-to-SPH mapping was 0.26 $M_\odot$ for 0.64-0.64 and 0.36$M_\odot$ for 0.81-0.81, as compared to 0.32 and 0.45 $M_\odot$ respectively in FLASH. This indicates that differences in ^{56}Ni production in FLASH and SPH are due to differences in post-contact conditions in the codes.

We find that collision simulations done with FLASH systematically produce less ^{56}Ni and more silicon-group elements than collisions done with SNSPH. This be-

havior was also noted by Rosswog et al. (2009), but the reason for the difference was not positively identified. We tentatively attribute this behavior to the post-shock temperature immediately after first contact. The SNSPH temperature is $\approx$10% higher than the FLASH temperature. Nuclear burning with a temperature sensitivity of T^{22} exacerbates the temperature difference, and causes the central regions in SNSPH to be more carbon depleted than in FLASH. With more carbon, the FLASH simulations runaway in the central region more easily and sooner, producing less ^{56}Ni. With less carbon, the SNSPH simulations runaway less easily, closer to the edges of the stalled shock region, and later in time, and thus produce more ^{56}Ni.

4.4 Expanded Reaction Network

In this work, a thirteen isotope alpha-chain reaction network is used, and ^{56}Ni is the primary observational signature studied. In future work, I will explore nucleosynthesis in SNIa explosions in-depth by post-processing the explosion ejecta using tracer particles in FLASH.

The FLASH passive tracer particles flow through the grid, and allow the properties of the grid to be tracked at each point in time. The density and temperature evolution of each tracer particle is tracked during the simulation, and used in post-processing to determine the nucleosynthesis experienced by the particle. The total yield is then the sum over all the tracer particles.

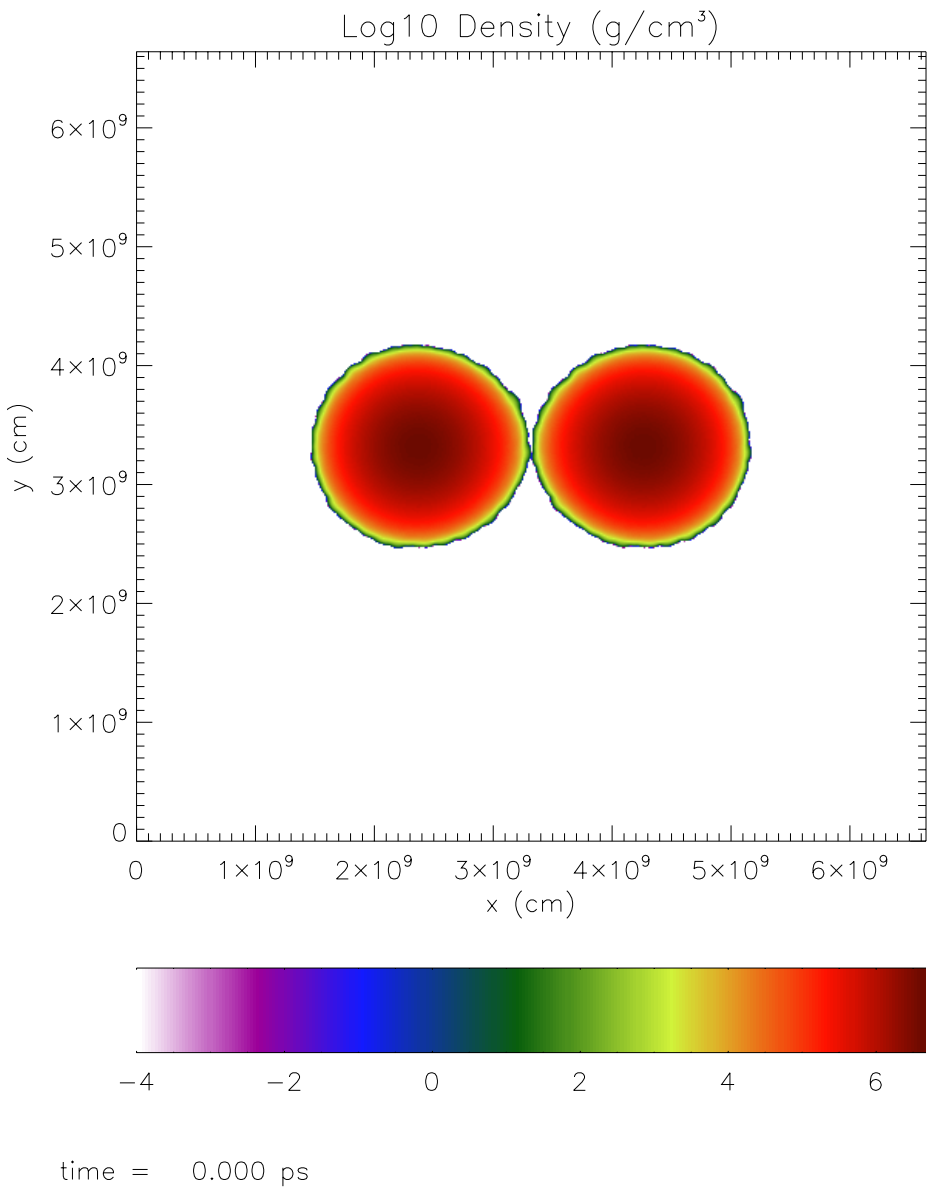

Figure 4.2: Initial mapping of density from SPH to FLASH for the 0.64-0.64 $M_{\odot}$ collision.

Altavilla, G., Ruiz-Lapuente, P., Balastegui, A., et al. 2009, ApJ, 695, 135

Benz, W., Cameron, A. G. W., Press, W. H., & Bowers, R. L. 1990, ApJ, 348, 647

Benz, W., Thielemann, F., & Hills, J. G. 1989, ApJ, 342, 986

Bianco, F. B., et al. 2011, ApJ, 741, 20

Blondin, S., et al. 2012, AJ, 143, 126

Branch, D., Fisher, A., & Nugent, P. 1993, AJ, 106, 2383

Branch, D., Livio, M., Yungelson, L. R., Boffi, F. R., & Baron, E. 1995, PASP, 107, 1019

Calder, A. C., et al. 2002, ApJS, 143, 201

Chandrasekhar, S. 1935, MNRAS, 95, 207

Chandrasekhar, S. 1984, Reviews of Modern Physics, 56, 137

Conley, A., et al. 2008, ApJ, 681, 482

da Silva, L. A. L. 1993, Ap&SS, 202, 215

Dan, M., Rosswog, S., Guillochon, J., & Ramirez-Ruiz, E. 2011, ApJ, 737, 89

—. 2012, MNRAS, 422, 2417

Feltzing, S., Holmberg, J., & Hurley, J. R. 2001, A&A, 377, 911

Filippenko, A. V., et al. 1992, AJ, 104, 1543

Foley, R. J., & Kasen, D. 2011, ApJ, 729, 55

Fryxell, B., et al. 2000, ApJS, 131, 273

Gallagher, J. S., Garnavich, P. M., Caldwell, N., Kirshner, R. P., Jha, S. W., Li, W., Ganeshalingam, M., & Filippenko, A. V. 2008, ApJ, 685, 752

Garnavich, P. M., et al. 2004, ApJ, 613, 1120

Gilfanov, M., & Bogdán, Á. 2010, Nature, 463, 924

Guerrero, J., García-Berro, E., & Isern, J. 2004, A&A, 413, 257

Guy, J., Astier, P., Nobili, S., Regnault, N., & Pain, R. 2005, A&A, 443, 781

Guy, J., et al. 2007, A&A, 466, 11

Hachinger, S., Mazzali, P. A., Taubenberger, S., Pakmor, R., & Hillebrandt, W. 2009, MNRAS, 399, 1238

Hamuy, M., Phillips, M. M., Suntzeff, N. B., Schommer, R. A., Maza, J., & Aviles, R. 1996, AJ, 112, 2391

Hamuy, M., et al. 1994, AJ, 108, 2226

Hicken, M., Garnavich, P. M., Prieto, J. L., Blondin, S., DePoy, D. L., Kirshner, R. P., & Parrent, J. 2007, ApJ, 669, L17

Hillebrandt, W., & Niemeyer, J. C. 2000, ARA&A, 38, 191

Howell, D. A. 2011, Nature Communications, 2

Howell, D. A., et al. 2006, Nature, 443, 308

—. 2009, ApJ, 691, 661

Iben, Jr., I., & Tutukov, A. V. 1984, ApJS, 54, 335

Jha, S., Riess, A. G., & Kirshner, R. P. 2007, ApJ, 659, 122

Jordan, IV, G. C., Fisher, R. T., Townsley, D. M., Calder, A. C., Graziani, C., Asida, S., Lamb, D. Q., & Truran, J. W. 2008, ApJ, 681, 1448

Kasen, D., Röpke, F. K., & Woosley, S. E. 2009, Nature, 460, 869

Khokhlov, A. M. 1991, A&A, 245, 114

Kim, A. G., Linder, E. V., Miquel, R., & Mostek, N. 2004, MNRAS, 347, 909

Leibundgut, B. 2001, ARA&A, 39, 67

Leibundgut, B., et al. 1993, AJ, 105, 301

Livio, M. 2000, in Type Ia Supernovae, Theory and Cosmology, ed. J. C. Niemeyer & J. W. Truran, 33

Livio, M. 2001, in Cosmic evolution, ed. E. Vangioni-Flam, R. Ferlet, & M. Lemoine, 299

Lorén-Aguilar, P., Isern, J., & García-Berro, E. 2009, A&A, 500, 1193

—. 2010, MNRAS, 406, 2749

Mannucci, F., Della Valle, M., & Panagia, N. 2006, MNRAS, 370, 773

Mannucci, F., Della Valle, M., Panagia, N., Cappellaro, E., Cresci, G., Maiolino, R., Petrosian, A., & Turatto, M. 2005, A&A, 433, 807

Maoz, D. 2008, MNRAS, 384, 267

Maoz, D. 2010, in American Institute of Physics Conference Series, Vol. 1314, American Institute of Physics Conference Series, ed. V. Kologera & M. van der Sluys, 223–232

Maoz, D., Mannucci, F., Li, W., Filippenko, A. V., Della Valle, M., & Panagia, N. 2011, MNRAS, 412, 1508

Marcello, D. C., & Tohline, J. E. 2012, ApJS, 199, 35

Mazzali, P. A., Chugai, N., Turatto, M., Lucy, L. B., Danziger, I. J., Cappellaro, E., della Valle, M., & Benetti, S. 1997, MNRAS, 284, 151

Mochkovitch, R., & Livio, M. 1989, A&A, 209, 111

Motl, P. M., Tohline, J. E., & Frank, J. 2002, ApJS, 138, 121

Mullally, F., Badenes, C., Thompson, S. E., & Lupton, R. 2009, ApJ, 707, L51

Napiwotzki, R., et al. 2007, in Astronomical Society of the Pacific Conference Series, Vol. 372, Astronomical Society of the Pacific Conference Series, ed. A. Napiwotzki & M. R. Burleigh, 387

Neill, J. D., et al. 2009, ApJ, 707, 1449

Nomoto, K., Thielemann, F.-K., & Yokoi, K. 1984, ApJ, 286, 644

Nomoto, K., Uenishi, T., Kobayashi, C., Umeda, H., Ohkubo, T., Hachisu, I., & Kato, M. 2003, in From Twilight to Highlight: The Physics of Supernovae, ed. W. Hillebrandt & B. Leibundgut, 115

Nugent, P. E., et al. 2011a, ArXiv e-prints

—. 2011b, Nature, 480, 344

Pakmor, R., Kromer, M., Röpke, F. K., Sim, S. A., Ruiter, A. J., & Hillebrandt, W. 2010, Nature, 463, 61

Pakmor, R., Kromer, M., Taubenberger, S., Sim, S. A., Röpke, F. K., & Hillebrandt, W. 2012, ApJ, 747, L10

Paxton, B., Bildsten, L., Dotter, A., Herwig, F., Lesaffre, P., & Timmes, F. 2011, ApJS, 192, 3

Perlmutter, S., et al. 1997, ApJ, 483, 565

—. 1999, ApJ, 517, 565

Pfahl, E., Scannapieco, E., & Bildsten, L. 2009, ApJ, 695, L111

Phillips, M. M. 1993, ApJ, 413, L105

Phillips, M. M., Lira, P., Suntzeff, N. B., Schommer, R. A., Hamuy, M., & Maza, J. 1999, AJ, 118, 1766

Piro, A. L., & Chang, P. 2008, ApJ, 678, 1158

Quimby, R., Höflich, P., & Wheeler, J. C. 2007, ApJ, 666, 1083

Rasio, F. A., & Shapiro, S. L. 1994, ApJ, 432, 242

—. 1995, ApJ, 438, 887

Raskin, C., Scannapieco, E., Rhoads, J., & Della Valle, M. 2008, ApJ, 689, 358

Raskin, C., Timmes, F. X., Scannapieco, E., Diehl, S., & Fryer, C. 2009, MNRAS, 399, L156

Raskin, C., Scannapieco, E., Rockefeller, G., Fryer, C., Diehl, S., & Timmes, F. X. 2010, ApJ, 724, 111

Raskin, C., Scannapieco, E., Fryer, C., Rockefeller, G., & Timmes, F. X. 2012, ApJ, 746, 62

Ricker, P. M. 2008, ApJS, 176, 293

Riess, A. G., Press, W. H., & Kirshner, R. P. 1996, ApJ, 473, 88

Riess, A. G., et al. 1998, AJ, 116, 1009

—. 2011, ApJ, 730, 119

Rosswog, S., Ramirez-Ruiz, E., & Hix, W. R. 2009, ApJ, 695, 404

Ruiter, A. J., Belczynski, K., & Fryer, C. 2009, ApJ, 699, 2026

Scalzo, R. A., et al. 2010, ApJ, 713, 1073

Scannapieco, E., & Bildsten, L. 2005, ApJ, 629, L85

Segretain, L., Chabrier, G., & Mochkovitch, R. 1997, ApJ, 481, 355

Shen, K. J., Bildsten, L., Kasen, D., & Quataert, E. 2012, ApJ, 748, 35

Silverman, J. M., et al. 2012, ArXiv e-prints

Spergel, D. N., et al. 2003, ApJS, 148, 175

Strigari, L. E. 2006, New A Rev., 50, 566

Sullivan, M., et al. 2006, ApJ, 648, 868

—. 2011, ApJ, 737, 102

Suzuki, N., et al. 2012, ApJ, 746, 85

Tanaka, M., et al. 2010, ApJ, 714, 1209

Taubenberger, S., et al. 2008, MNRAS, 385, 75

Thielemann, F.-K., Nomoto, K., & Yokoi, K. 1986, A&A, 158, 17

Timmes, F. X., Woosley, S. E., & Weaver, T. A. 1995, ApJS, 98, 617

Timmes, F. X. 1999, ApJS, 124, 241

Timmes, F. X., & Swesty, F. D. 2000, ApJS, 126, 501

Timmes, F. X., & Woosley, S. E. 1992, ApJ, 396, 649

Townsley, D. M., Jackson, A. P., Calder, A. C., Chamulak, D. A., Brown, E. F., & Timmes, F. X. 2009, ApJ, 701, 1582

Turatto, M., Benetti, S., Cappellaro, E., Danziger, I. J., Della Valle, M., Gouiffes, C., Mazzali, P. A., & Patat, F. 1996, MNRAS, 283, 1

van Kerkwijk, M. H., Chang, P., & Justham, S. 2010, ApJ, 722, L157

Wang, B., & Han, Z. 2012, New A Rev., 56, 122

Webbink, R. F. 1984, ApJ, 277, 355

Wheeler, J. C., Sneden, C., & Truran, J. W., Jr. 1989, ARA&A, 27, 279

Whelan, J., & Iben, I. J. 1973, ApJ, 186, 1007

Woosley, S. E., Kerstein, A. R., & Aspden, A. J. 2011, ApJ, 734, 37

Woosley, S. E., & Weaver, T. A. 1986, ARA&A, 24, 205

Woosley, S. E., Wunsch, S., & Kuhlen, M. 2004, ApJ, 607, 921

Yamanaka, M., et al. 2009, ApJ, 707, L118

Yoon, S.-C., Podsiadlowski, P., & Rosswog, S. 2007, MNRAS, 380, 933